Structural Basis of Mitochondrial Receptor Binding and GTP-Driven Conformational Constriction by Dynamin-Related Protein 1

Raghav Kalia[1,2,3,5], Ray Yu-Ruei Wang[1,3,4], Ali Yusuf[1,3], Paul V. Thomas[1,3,5], David A. Agard[1,3,4], Janet M. Shaw[2,4], and Adam Frost[1,2,3,5]

[1]Department of Biochemistry and Biophysics, University of California, San Francisco, San Francisco, CA 94158 USA

[2]Department of Biochemistry, University of Utah, Salt Lake City, UT, 84112 USA

[3]California Institute for Quantitative Biomedical Research, San Francisco, CA 94158 USA

[4]Howard Hughes Medical Institute

[5]Chan Zuckerberg Biohub, San Francisco, CA 94158 USA

Corresponding author. Email: adam.frost@ucsf.edu

Abstract

Mitochondrial inheritance, genome maintenance, and metabolic adaptation all depend on organelle fission by Dynamin-Related Protein 1 (DRP1) and its mitochondrial receptors. DRP1 receptors include the paralogs Mitochondrial Dynamics 49 and 51 (MID49/MID51) and Mitochondrial Fission Factor (MFF), but the mechanisms by which these proteins recruit DRP1 and regulate its activities are unknown. Here we present a cryoEM structure of human, full-length DRP1 bound to MID49 and an analysis of structure- and disease-based mutations. We report that GTP binding allosterically induces a remarkable elongation and rotation of the G-domain, Bundle-Signaling Element (BSE) and connecting hinge loops of DRP1. In this nucleotide-bound conformation, a distributed network of multivalent interactions promotes DRP1 copolymerization into a linear filament with MID49, MID51 or both. Subsequent GTP hydrolysis and exchange within the filament leads to receptor dissociation, shortening through disassembly, and concomitant curling of DRP1 oligomers into closed rings. The dimensions of the closed DRP1 rings are consistent with DRP1-constricted mitochondrial tubules observed in human cells. These structures are the first views of full-length, receptor- and nucleotide-bound dynamin-family GTPases and—in comparison with nucleotide-free crystal structures—teach us how these molecular machines perform mechanical work through nucleotide-driven allostery.

36 **Introduction**

37 Pioneering work in yeast and other model systems revealed that fragmentation of
38 the mitochondrial reticulum disperses units of the organelle during cell division[1-3],
39 coordinates morphological adaptation with metabolic demand[4-7], and quarantines
40 damaged units for turnover[8-10]. Recent work also led to the discovery of the role
41 mitochondrial fission plays in regulated cell death pathways[11-19], brain development and
42 synaptic function[20-23], and how certain pathogens disrupt these processes and hijack
43 mitochondrial resources[24-26]. Finally, there is a growing understanding of how inter-
44 organelle contacts between the ER and mitochondria initiate mitochondrial fission[27,28],
45 and how this process regulates mitochondrial genome duplication and integrity[29,30]. The
46 master regulator that unites these processes across eukaryotic evolution is the
47 membrane-remodeling GTPase DRP1[4,7,31-37].

48 DRP1 is necessary but not sufficient for mitochondrial fission because receptor
49 proteins must recruit the enzyme to the Outer Mitochondrial Membrane (OMM). In
50 mammals, these include the paralogs MItochondrial Dynamics proteins MID49 and
51 MID51 or the Mitochondrial Fission Factor, MFF [32,35,38-41]. Following receptor-dependent
52 recruitment, DRP1 assembles into polymers that encircle mitochondria and, through still
53 poorly understood mechanisms, channels energy from GTP binding, hydrolysis, and
54 nucleotide exchange into a mechanochemical constriction[13,41-46]. In addition to DRP1 and

55 its OMM receptors, a recent study revealed that a second member of the dynamin-family
56 of GTPases, dynamin-2, enacts the final fission event downstream of DRP1-driven
57 constriction of a mitochondrial tubule[47]. Thus, mitochondrial division is a stepwise reaction
58 regulated by DRP1 receptor binding, oligomerization and nucleotide-dependent
59 conformational dynamics.

60 We and others have reported that the OMM receptors MFF or MID49/51 are
61 independently sufficient to recruit DRP1 in order to divide mitochondria[38,39,41,48]. We also
62 reported that MID49/51 can coassemble with DRP1 forming a copolymer with a
63 dramatically different morphology than reported for dynamin-family members[41]. While
64 these results suggest that an adaptor protein could alter the architecture of a dynamin
65 polymer to facilitate a mitochondria-specific activity, the architecture and functions of this
66 coassembly remain unclear.

67 Here, we report the structural basis of DRP1 coassembly with MID49/MID51. Our
68 cryoEM structure reveals how nucleotide binding to the G-domain induces conformational
69 changes that allosterically propagate through the BSE to open and elongate DRP1 and
70 thereby expose multiple receptor-binding surfaces. MID49/51 binding stabilizes a specific
71 alignment of DRP1 tetramers to nucleate polymerization of a linear co-filament. Then, in
72 a path-dependent reaction, we show how GTP hydrolysis and nucleotide exchange lead
73 to conformational constriction by the polymer. Specifically, when DRP1 subunits within

74 the cofilament exchange and hydrolyze nucleotide, they dissociate from MID49/51
75 receptors and the entire polymer dynamically shortens and curls into a closed ring.
76 Analysis of structure-based and disease-causing mutations indicate that allosterically
77 driven rearrangements of the stalk helices—and the critical L1N^{S} loop—support curling
78 from linear strings into constricted rings following receptor dissociation.
79

80 **Results and Discussion**

81 To date, many structural studies of dynamin-family proteins have relied upon
82 mutated or truncated constructs to facilitate crystallization. We purified wild-type, full-
83 length human DRP1 including the N-terminal GTPase domain (G-domain), Bundle
84 Signaling Element (BSE), and four-helix bundle known as the stalk (Fig. 1a). This
85 construct also contained the lipid binding ~100 amino acid region referred to as the
86 variable domain (VD) that sits between the third and fourth alpha helices of the stalk,
87 analogous to the Pleckstrin Homology (PH) domain found in endocytic dynamin proteins.
88 A crystal structure of a nucleotide-free and truncated DRP1 mutant revealed the
89 organization of these domains and an overall similarity with the structure of nucleotide-
90 free endocytic dynamin[42,49,50]. We also purified soluble truncations of MID49 and MID51
91 engineered to lack their N-terminal transmembrane anchors but include the cytoplasmic

92 nucleotidyltransferase-like domain and the "Dynamin Recruitment Region" (DRR)
93 required for DRP1 binding (Fig 1a)[38,51-54].

94 Incubating equimolar ratios of DRP1 with soluble $MID49_{126-454}$, $MID51_{132-463}$, or
95 both proteins together, in the presence of GTP resulted in cofilament assembly (Extended
96 Data Figs. 1-2). We focused on the filaments formed with $MID49_{126-454}$ in the presence of
97 the non-hydrolyzable analog GMPPCP and determined their structure from cryoEM
98 images (Extended Data Figs. 3-9 and Table 1). 3D reconstruction resolved elongated
99 DRP1 dimers bound stoichiometrically to $MID49_{126-454}$, without assignable density for the
100 variable domain (Fig. 1b, Extended Data Fig. 4). Surprisingly, each chain of DRP1 bound
101 MID49 at four different sites, and each MID49 in turn bound four DRP1 molecules to yield
102 a vast and highly avid interaction network (Figs. 1b-c, Extended Data Figs. 4 and 8).
103 MID49 binding to four separate DRP1 molecules stabilized a linear arrangement of inter-
104 DRP1 interfaces reminiscent of those observed for other dynamin-family proteins by X-
105 ray crystallography (Fig. 1b, Extended Data Figs. 4 and 8)[42,49,50,55-57].

106 MID49's DRR motif occupied the space between two neighboring G-domains and
107 contacted both via MID-interaction interfaces 1 and 2 (buried surface areas of ~530$Å^2$
108 and ~200 $Å^2$, respectively, see Fig. 1b-d). The precise spacing required for this bivalent
109 G-domain interaction explains why previous mutagenesis efforts suggested that the size
110 and topology of the β4–α4 loop, rather than its exact sequence (which differs between

111 MID49 and MID51) are critical determinants of binding. Single point mutations within this
112 loop for MID49 and MID51 did not disrupt binding, while mutations that altered the length,
113 topology or positioning of the loop did[51,52,54]. We found that mutating conserved DRP1
114 residues involved in interface 1—the energetically most significant interface—did prevent
115 coassembly. Specifically, the D190A mutation should neutralize an interface 1 salt bridge
116 and the D221A mutation should alter the conformation of an interface 1 loop (Fig. 1d).
117 We observed that both mutants prevented assembly with MID49 and altered DRP1's self-
118 assembly properties (Extended Data Figs. 10-12).

119 Unexpectedly, MID49 also made contact with the stalk loops of a third and fourth
120 DRP1 molecule through MID-interaction interfaces 3 and 4 (buried surface areas of
121 ~450Å^2 and ~230Å^2, respectively, Fig. 1c, e, and f). The loops involved in both interaction
122 interfaces 3 and 4 determine the assembly properties of higher-order dynamin-family
123 oligomers [42,49,50,55-57]. MID-interaction surface 3, in particular, harbors the conserved loop
124 L1N^S and is the site of multiple disease alleles that lead to elongated mitochondrial
125 morphology, including G362D and G363D (Fig. 1e, Extended Data Figs. 10-11 and [58-60]).
126 Prior work has also established that this loop comprises part of the intra-molecular PH
127 domain binding site for the soluble state of endocytic dynamin tetramers (Extended Data
128 Fig. 13)[57], and is a determinant of conformational heterogeneity for these and other
129 dynamin-family proteins[55,57,61]. The presence of disease alleles near this interface

130 suggests that these mutations may compromise receptor interactions and that defects in
131 the recruitment of DRP1 to mitochondria may contribute to pathogenesis. As discussed
132 below, we found that the G362D mutant (Fig. 1e) failed to coassemble with MID49 and
133 displayed altered assembly and conformational properties (Extended Data Figs. 12-15).

134 Understanding the allosteric coupling between nucleotide binding, hydrolysis or
135 exchange and the conformational repertoire of dynamin-family GTPases remains an
136 unmet challenge[62,63]. We observed that the GMPPCP-bound G-domains and the BSE of
137 DRP1 adopt strikingly different conformations in the cryoEM density compared to the
138 nucleotide-free crystal structure[42]. In addition to other nucleotide-induced conformational
139 changes within the G-domain, the most salient are the closing of the G2/switch-1 loop to
140 form a closed "lid" over the nucleotide (Figs. 2a-c). The closure of the switch-1 lid
141 propagates through the adjacent beta sheet to push the α-helices of the BSE into an
142 orthogonal position (Extended Data Movie 1). When evaluated in the context of a stalk
143 interface-2 DRP1 dimer, this conformational change is an impressive 90° rotation of the
144 G-domain and a 40Å translation toward the stalk (Fig. 2d, Extended Data Movies 2-3).
145 Two of the three DRP1 surfaces that engage the DRR of MID49 (MID receptor interaction
146 interfaces 1 and 2, Figs. 1-2) are inaccessible in the nucleotide-free state but become
147 available for binding upon nucleotide-driven elongation (Fig. 2d, Extended Data Movies
148 2-3).

149 Since DRP1's ability to polymerize into linear filaments with MID49 or MID51
150 depended on non-hydrolyzable GTP analogs, we next evaluated the dynamics of these
151 filaments in the presence of hydrolyzable GTP. Following copolymerization in the
152 presence of the non-hydrolyzable analog, we exchanged GMPPCP for GTP through
153 dialysis and followed the reaction using negative stain transmission electron microscopy
154 at sequential time points until the GTP was exhausted. We observed that the linear DRP1-
155 MID49 cofilaments disassembled into small oligomers upon complete hydrolysis to GDP
156 and exhibited a fascinating dynamic instability at intermediate time points (Fig. 3).
157 Specifically, the long and linear filaments seen at early time points disassembled into
158 shorter, curling oligomers that—upon reaching a reproducibly narrow range of lengths—
159 spontaneously closed into constricted rings that were remarkably uniform in diameter
160 (Fig. 3).

161 In a separate but related experiment, we evaluated the assembly properties of the
162 DRP1 mutant G362D with and without $MID49_{126-454}$. As described above, this disease-
163 associated residue sits at the base of the $L1N^S$ loop that forms part of the third interface
164 with MID49 (Figs. 1c, 1e, Extended Data Fig. 13). We found that $DRP1_{G362D}$ purified as a
165 nearly monodisperse and stable dimer, rather than a mix of tetramers and higher order
166 species observed for the wild-type, full-length protein (Extended Data Fig. 12). In addition,
167 $DRP1_{G362D}$ exclusively formed rings, not filaments, with or without $MID49_{126-454}$ and in the

168 presence of GMPPCP or GTP (Fig. 4a, Extended Data Figs. 14-15). These rings
169 resembled those observed with wild-type DRP1 in all respects except that the wild-type
170 protein only formed closed rings from the pre-formed linear MID49 copolymers through
171 the path-dependent reaction described above (Fig. 3 versus Fig. 4). Using the non-
172 hydrolyzable GTP analog GMPPCP with the $DRP1_{G362D}$ rings also improved structural
173 homogeneity, presumably because the wild-type rings remain dynamic and eventually
174 disassembled in the presence of GTP upon complete hydrolysis to GDP (Fig. 3).

175 We imaged the $DRP1_{G362D}$ rings using cryoEM and used 2D class averages of the
176 predominant 12-dimer closed ring to model the architectural differences between the
177 linear filaments and the closed rings (Fig. 4, Extended Data Fig. 14-15). To account for
178 the projected ring density, the G-domain and the BSE of DRP1 must move even further
179 down toward the stalks. Moreover, while stalk interface-2 remains constant—as revealed
180 by the X-shaped projected dimer (Fig. 4c)—the curvature of the ring dictates that stalk
181 interfaces 1 and 3 must be extensively remodeled to allow a ~30 degree bending per
182 dimer in comparison with the linear DRP1-MID49 copolymer (Fig. 4d, Extended Data Fig.
183 15, Movie 4). We did not observe any density for MID49 in the wild-type rings that form
184 by curling of the MID49-DRP1 cofilament in the presence of GTP, nor in our higher-
185 resolution analysis of the $DRP1_{G362D}$ rings that form with or without MID49 present (Fig.
186 4b-c, Extended Data Fig. 14-15).

187 We note that even the most constricted form of the closed ring is insufficient to
188 drive complete mitochondrial fission because the inner diameter is only ~16nm. This
189 length suggests that a constricted membrane tubule would be stable and that the
190 structures we have observed in vitro could correspond with the highly-constricted but pre-
191 fission state observed in living cells when another dynamin-family protein, the primarily
192 endocytic dynamin-2, is depleted[47]. Thus, initial constriction by DRP1 may stabilize the
193 high degree of membrane curvature that is suitable, perhaps even tuned, for the
194 recruitment and final fission event catalyzed by additional dynamin-family enzymes.

195 Together, these findings establish four conceptual advances. First, our cryoEM
196 structure revealed how receptor proteins like MID49/MID51 recruit and stabilize a specific
197 nucleotide-bound conformation of DRP1 and nucleate polymerization of a cofilament. We
198 speculate that the nearly linear properties of this polymer have adapted to encircle low-
199 curvature mitochondrial tubules. The selective stabilization of this open, elongated
200 conformation of DRP1 within the MID receptor cofilament explains why overexpression
201 of the MID receptors inhibits mitochondrial fission[39]. Second, analysis of the MID49-DRP1
202 copolymer exposed how nucleotide binding induces an impressive conformational
203 rearrangement to expose a network of multi-valent receptor binding sites. We now
204 understand these nucleotide-driven allosteric transformations in detail and in the context
205 of full-length and oligomeric DRP1. Third, a path-dependent constriction reaction revealed

206 intrinsic GTP-dependent DRP1 properties that are reminiscent of microtubule dynamic
207 instability[64]. In this reaction, nucleotide exchange and hydrolysis led to MID49/51 receptor
208 dissociation, disassembly from the ends of the linear filament, and concomitant curling of
209 the shortened filaments into closed rings. Fourth and finally, analysis of a disease mutant
210 in the $L1N^S$ loop, $DRP1_{G362D}$, exposed this loop as a vital determinant of mitochondrial
211 receptor binding and the dynamic inter-stalk interactions that govern oligomer architecture
212 and the ability of dynamin proteins to perform mechanical work.
213

214 **Acknowledgments**

215 We thank Michael Braunfeld, Cameron Kennedy, David Bulkley, and Alexander
216 Myasnikov and the UCSF Center for Advanced CryoEM, which is supported in part from
217 NIH grants S10OD020054 and 1S10OD021741 and the Howard Hughes Medical
218 Institute. We also thank the QB3 shared cluster and NIH grant 1S10OD021596-01, Jean-
219 Paul Armache, Nathaniel Talledge for microscopy advice, and Charles Greenberg for
220 consulting on structural modeling. This work was further supported by a Faculty Scholar
221 grant from the Howard Hughes Medical Institute (A.F.), the Searle Scholars Program
222 (A.F.), NIH grant 1DP2GM110772-01 (A.F.), NIH grants GM53466 and GM84970 (J.S.),
223 and the Howard Hughes Medical Institute (R.W., J.S., D.A.). A.F. is a
224 Chan Zuckerberg Biohub investigator.
225
226

227 **Author Contributions**

228 R.K., J.S. and A.F. conceived of the study. R.K., R.W., A.Y. and P.T. performed all
229 experiments. R.K., R.W. and A.F. performed the computational analyses. All authors
230 evaluated the results and edited the manuscript. R.K. and A.F. wrote the manuscript with
231 input from all of the authors.

232

233 **Data Accessibility:**

234 All of the cryoEM density maps associated with this study have be deposited in the EMDB
235 with accession numbers EMD-8874(PROC). The atomic coordinates have been
236 deposited in the PDB as 5WP9(PROC).

Figures

Kalia, et al.
Figure 1

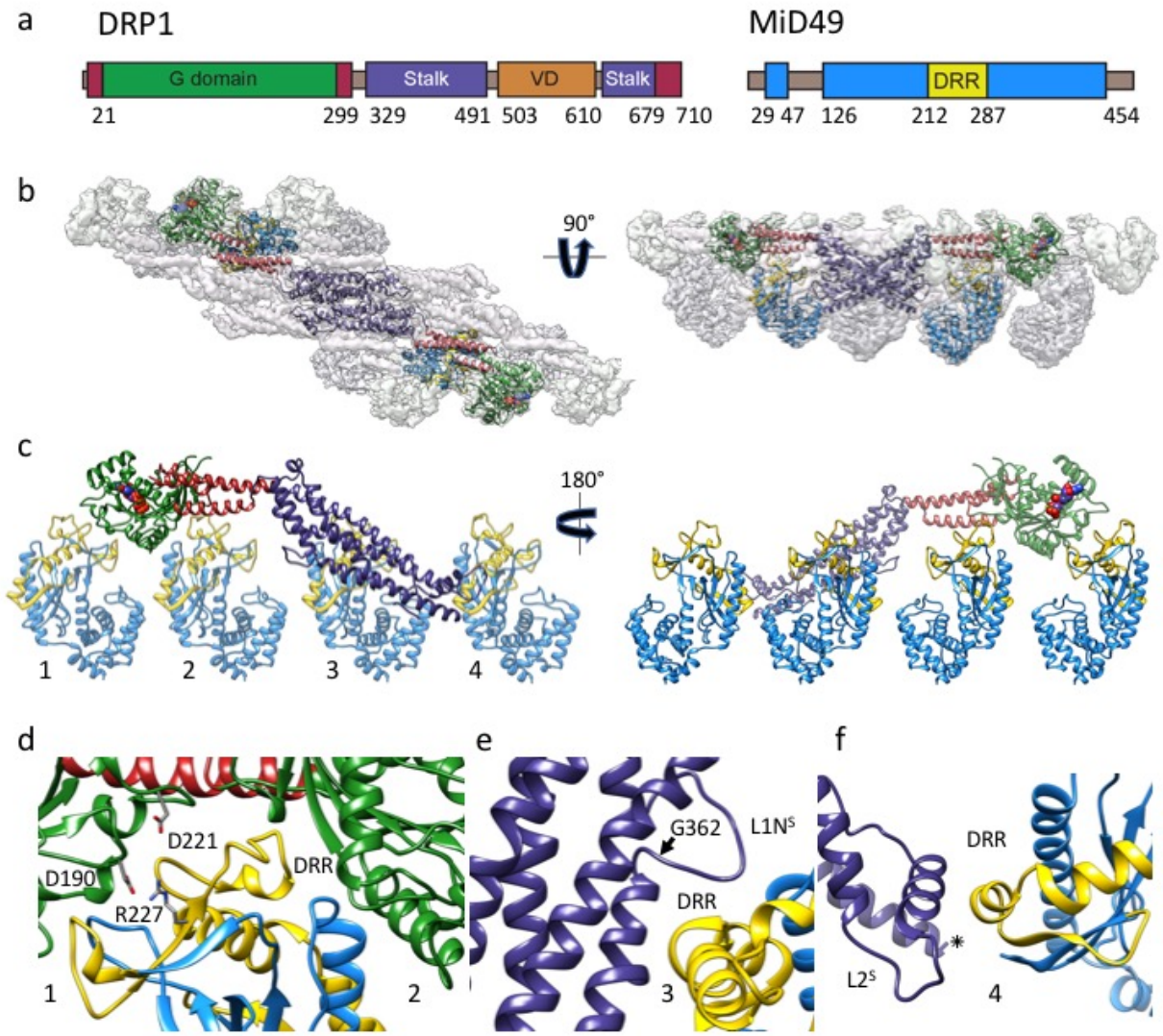

239 **Figure 1: Architecture of the DRP1-MID49 linear filament:** (**a**) DRP1 and MID49
240 domain arrangements. (**b**) Density map and atomic models for DRP1 and $MID49_{126-454}$.
241 Green: G-domain, Red: Bundle Signaling Element (BSE), Purple: Stalk, Blue: MID49,
242 Yellow: Dynamin Recruitment Region (DRR) of MID49. (**c**) Each DRP1 chain contacts
243 four different MID49 molecules, as numbered. (**d**) MID-interaction surfaces 1 and 2.
244 Green ribbons on either side of the DRR come from two separate G-domains, and the
245 residues involved in a key salt bridge for MID-interaction surface 1 are shown as sticks.
246 (**e**) Rotated view of MID-interaction surface 3. Disease-associated DRP1 residue G362
247 (arrow) supports the conformation of the $L1N^S$ loop essential for linear copolymerization
248 with MID receptors. (**f**) Rotated view of MID-interaction surface 4 and the $L2^S$ loop.
249
250
251
252
253
254
255
256
257

Kalia, et al.
Figure 2

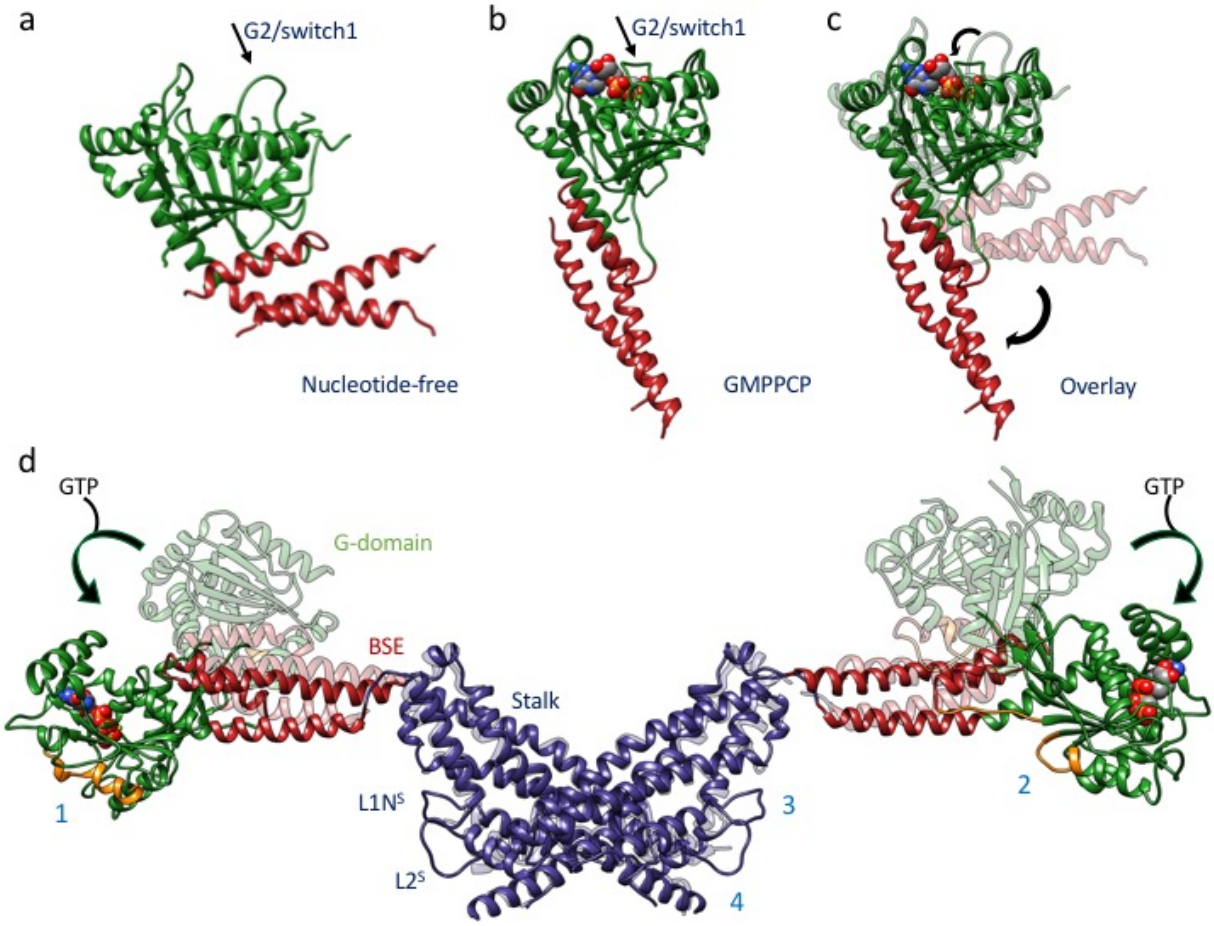

Figure 2: Nucleotide-driven allosteric elongation of DRP1 exposes MID binding sites: **(a)** nucleotide-free state of DRP1 G-domain and BSE as seen in a crystal structure (PDB ID: 4BEJ). Arrow points to the G2/switch1 loop. **(b)** GMPPCP-bound G-domain-BSE conformation determined by cryoEM. **(c)** Overlay of A and B. Curved arrows highlight the closing of G2/switch 1 “lid” and the opening of the BSE “wrist”. **(d)** Global conformational change induced by nucleotide binding. Rotation and translation of the G-domain and BSE elongates the dimer and exposes MID-interaction surfaces 1 and 2 (annotated on separate monomers for clarity). The surfaces of the G-domains that engage MID receptors are rendered orange in the nucleotide-bound and elongated conformation.

Kalia, et al.
Figure 3

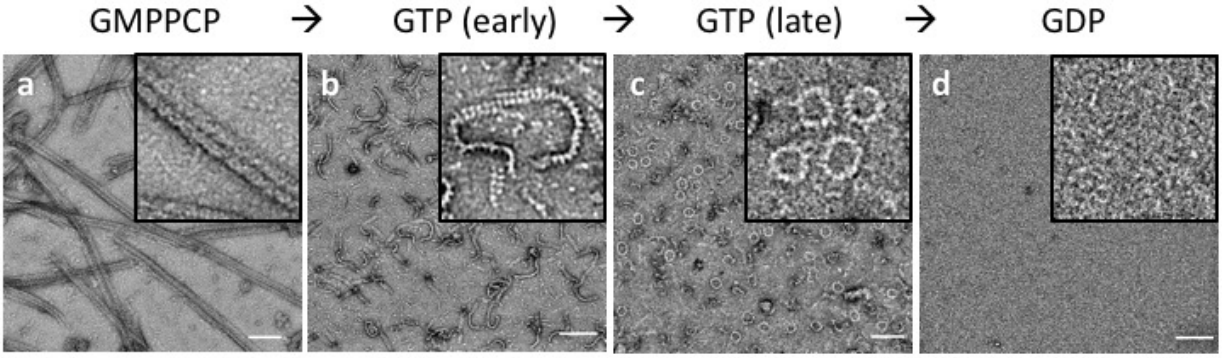

279 **Figure 3: Dynamic instability of the DRP1-MID49 linear assembly and curling into**

280 **closed DRP1 rings**: **(a)** DRP1-MID49$_{126-454}$ linear filaments copolymerized with

281 GMPPCP. **(b-c)** Subsequent exchange into GTP leads to partial disassembly and curling

282 into closed rings. **(d)** GTP exhaustion leads to complete oligomer disassembly.

283 Bars=100nm.

284

285

286

287

288

289

290

291

292

293

294

295

296

297

Kalia, et al.
Figure 4

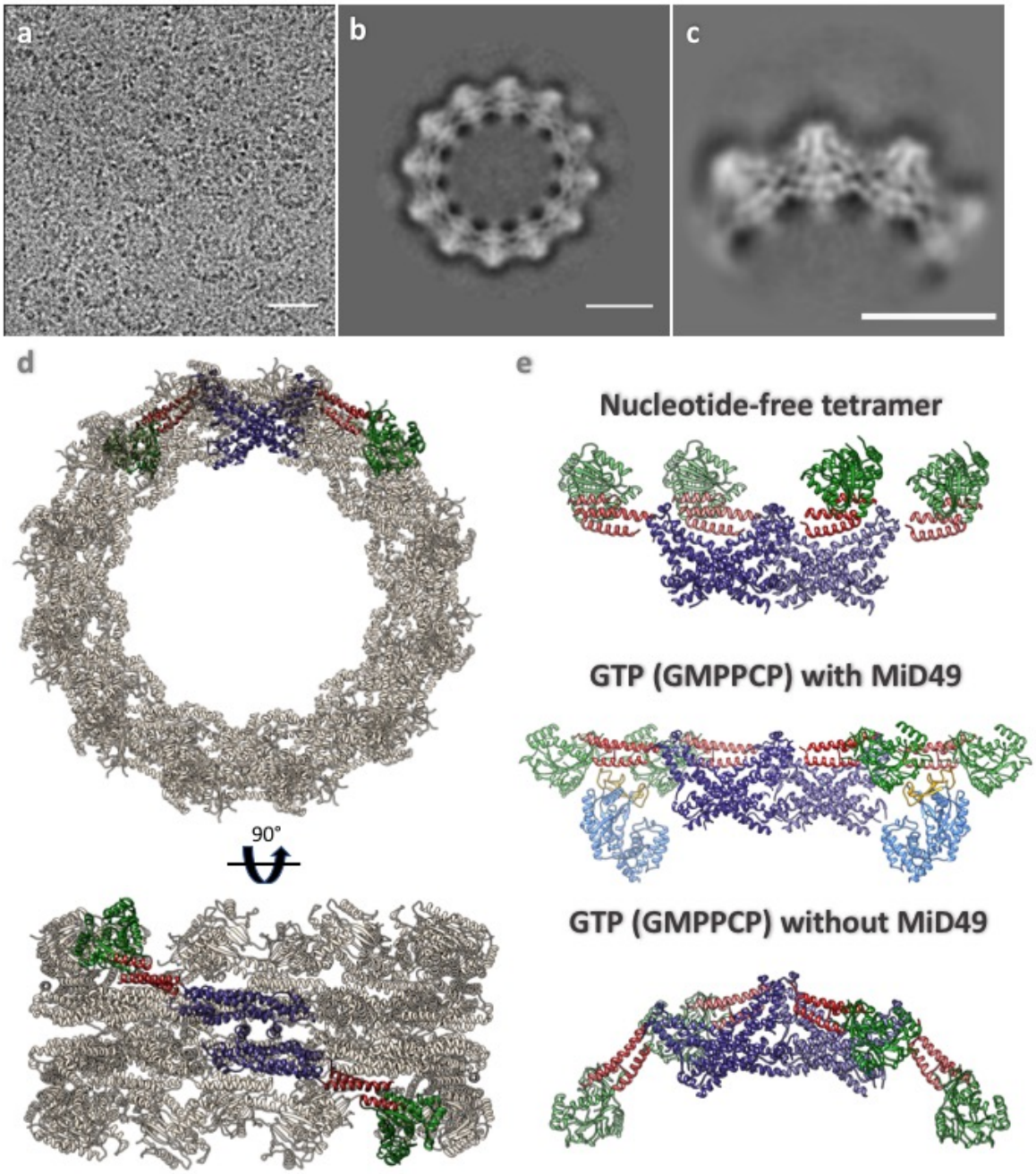

299 **Figure 4: DRP1$_{G362D}$ cannot bind MID49 and forms rings exclusively with GMPPCP**

300 **or GTP. (a)** CryoEM micrograph of DRP1$_{G362D}$ rings. **(b)** 2D class average of the

301 predominant closed ring that comprises 12 DRP1 dimers. **(c)** 2D class average of a

302 quarter of the ring revealing the secondary structure elements of the "X"-shaped DRP1

303 dimer. **(d)** 3D model of the closed ring. **(e)** Comparison between DRP1 tetramers

304 observed in the nucleotide-free state (top, PDB ID: 4BEJ), the GMPPCP and MID49$_{126-}$

305 $_{454}$-bound linear state (middle), and the bent conformation modeled for the rings. Bar for

306 **(a)** = 30nm, for **(b, c)** =100Å.

Extended Data

Methods

Figures 1 to 15

Movies 1 to 4

Table 1

Extended Data References

314 **References**

315 1 Mishra, P. & Chan, D. C. Mitochondrial dynamics and inheritance during cell division,
316 development and disease. *Nature reviews. Molecular cell biology* **15**, 634-646,
317 doi:10.1038/nrm3877 (2014).
318 2 Jourdain, I., Gachet, Y. & Hyams, J. S. The dynamin related protein Dnm1 fragments
319 mitochondria in a microtubule-dependent manner during the fission yeast cell cycle. *Cell*
320 *Motil Cytoskeleton* **66**, 509-523, doi:10.1002/cm.20351 (2009).
321 3 Kanfer, G. & Kornmann, B. Dynamics of the mitochondrial network during mitosis.
322 *Biochem Soc Trans* **44**, 510-516, doi:10.1042/BST20150274 (2016).
323 4 Toyama, E. Q. *et al.* Metabolism. AMP-activated protein kinase mediates mitochondrial
324 fission in response to energy stress. *Science (New York, N.Y.)* **351**, 275-281,
325 doi:10.1126/science.aab4138 (2016).
326 5 Roy, M., Reddy, P. H., Iijima, M. & Sesaki, H. Mitochondrial division and fusion in
327 metabolism. *Current opinion in cell biology* **33**, 111-118, doi:10.1016/j.ceb.2015.02.001
328 (2015).
329 6 Picard, M., Juster, R. P. & McEwen, B. S. Mitochondrial allostatic load puts the 'gluc' back
330 in glucocorticoids. *Nat Rev Endocrinol* **10**, 303-310, doi:10.1038/nrendo.2014.22 (2014).
331 7 Mishra, P. & Chan, D. C. Metabolic regulation of mitochondrial dynamics. *The Journal of*
332 *cell biology* **212**, 379-387, doi:10.1083/jcb.201511036 (2016).
333 8 Twig, G. *et al.* Fission and selective fusion govern mitochondrial segregation and
334 elimination by autophagy. *Embo J* **27**, 433-446, doi:10.1038/sj.emboj.7601963 (2008).
335 9 Frank, M. *et al.* Mitophagy is triggered by mild oxidative stress in a mitochondrial fission
336 dependent manner. *Biochim Biophys Acta* **1823**, 2297-2310,
337 doi:10.1016/j.bbamcr.2012.08.007 (2012).
338 10 Mao, K. & Klionsky, D. J. Mitochondrial fission facilitates mitophagy in Saccharomyces
339 cerevisiae. *Autophagy* **9**, 1900-1901, doi:10.4161/auto.25804 (2013).
340 11 Chan, D. C. Fusion and fission: interlinked processes critical for mitochondrial health.
341 *Annu Rev Genet* **46**, 265-287, doi:10.1146/annurev-genet-110410-132529 (2012).
342 12 Lee, H. & Yoon, Y. Mitochondrial fission: regulation and ER connection. *Mol Cells* **37**, 89-
343 94, doi:10.14348/molcells.2014.2329 (2014).
344 13 van der Bliek, A. M., Shen, Q. & Kawajiri, S. Mechanisms of mitochondrial fission and
345 fusion. *Cold Spring Harb Perspect Biol* **5**, doi:10.1101/cshperspect.a011072 (2013).
346 14 Sheridan, C. & Martin, S. J. Mitochondrial fission/fusion dynamics and apoptosis.
347 *Mitochondrion* **10**, 640-648, doi:10.1016/j.mito.2010.08.005 (2010).
348 15 Parone, P. A. & Martinou, J. C. Mitochondrial fission and apoptosis: an ongoing trial.
349 *Biochim Biophys Acta* **1763**, 522-530, doi:10.1016/j.bbamcr.2006.04.005 (2006).
350 16 Youle, R. J. & Karbowski, M. Mitochondrial fission in apoptosis. *Nature reviews.*
351 *Molecular cell biology* **6**, 657-663, doi:10.1038/nrm1697 (2005).
352 17 Perfettini, J. L., Roumier, T. & Kroemer, G. Mitochondrial fusion and fission in the control
353 of apoptosis. *Trends in cell biology* **15**, 179-183, doi:10.1016/j.tcb.2005.02.005 (2005).
354 18 Oakes, S. A. & Korsmeyer, S. J. Untangling the web: mitochondrial fission and apoptosis.
355 *Dev Cell* **7**, 460-462, doi:10.1016/j.devcel.2004.09.010 (2004).

356 19 Frank, S. *et al.* The role of dynamin-related protein 1, a mediator of mitochondrial
357 fission, in apoptosis. *Dev Cell* **1**, 515-525 (2001).
358 20 Ishihara, N. *et al.* Mitochondrial fission factor Drp1 is essential for embryonic
359 development and synapse formation in mice. *Nature cell biology* **11**, 958-966,
360 doi:10.1038/ncb1907 (2009).
361 21 Wakabayashi, J. *et al.* The dynamin-related GTPase Drp1 is required for embryonic and
362 brain development in mice. *Journal of Cell Biology* **186**, 805-816,
363 doi:10.1083/jcb.200903065 (2009).
364 22 Kageyama, Y. *et al.* Parkin-independent mitophagy requires Drp1 and maintains the
365 integrity of mammalian heart and brain. *Embo J* **33**, 2798-2813,
366 doi:10.15252/embj.201488658 (2014).
367 23 Schwarz, T. L. Mitochondrial trafficking in neurons. *Cold Spring Harb Perspect Biol* **5**,
368 doi:10.1101/cshperspect.a011304 (2013).
369 24 Chatel-Chaix, L. *et al.* Dengue Virus Perturbs Mitochondrial Morphodynamics to Dampen
370 Innate Immune Responses. *Cell Host Microbe* **20**, 342-356,
371 doi:10.1016/j.chom.2016.07.008 (2016).
372 25 Welsch, S. *et al.* Composition and three-dimensional architecture of the dengue virus
373 replication and assembly sites. *Cell Host Microbe* **5**, 365-375,
374 doi:10.1016/j.chom.2009.03.007 (2009).
375 26 Kim, S. J. *et al.* Hepatitis B virus disrupts mitochondrial dynamics: induces fission and
376 mitophagy to attenuate apoptosis. *PLoS Pathog* **9**, e1003722,
377 doi:10.1371/journal.ppat.1003722 (2013).
378 27 Friedman, J. R. *et al.* ER tubules mark sites of mitochondrial division. *Science (New York,*
379 *N.Y.)* **334**, 358-362, doi:10.1126/science.1207385 (2011).
380 28 Murley, A. *et al.* ER-associated mitochondrial division links the distribution of
381 mitochondria and mitochondrial DNA in yeast. *eLife* **2**, e00422, doi:10.7554/eLife.00422
382 (2013).
383 29 Lewis, S. C., Uchiyama, L. F. & Nunnari, J. ER-mitochondria contacts couple mtDNA
384 synthesis with mitochondrial division in human cells. *Science (New York, N.Y.)* **353**,
385 aaf5549, doi:10.1126/science.aaf5549 (2016).
386 30 Osman, C., Noriega, T. R., Okreglak, V., Fung, J. C. & Walter, P. Integrity of the yeast
387 mitochondrial genome, but not its distribution and inheritance, relies on mitochondrial
388 fission and fusion. *Proc Natl Acad Sci U S A* **112**, E947-956,
389 doi:10.1073/pnas.1501737112 (2015).
390 31 Chang, C. R. & Blackstone, C. Dynamic regulation of mitochondrial fission through
391 modification of the dynamin-related protein Drp1. *Ann N Y Acad Sci* **1201**, 34-39,
392 doi:10.1111/j.1749-6632.2010.05629.x (2010).
393 32 Elgass, K., Pakay, J., Ryan, M. T. & Palmer, C. S. Recent advances into the understanding
394 of mitochondrial fission. *Biochim Biophys Acta* **1833**, 150-161,
395 doi:10.1016/j.bbamcr.2012.05.002 (2013).
396 33 Otera, H., Ishihara, N. & Mihara, K. New insights into the function and regulation of
397 mitochondrial fission. *Biochim Biophys Acta* **1833**, 1256-1268,
398 doi:10.1016/j.bbamcr.2013.02.002 (2013).

399 34 Prudent, J. *et al.* MAPL SUMOylation of Drp1 Stabilizes an ER/Mitochondrial Platform
400 Required for Cell Death. *Molecular cell* **59**, 941-955, doi:10.1016/j.molcel.2015.08.001
401 (2015).
402 35 Bui, H. T. & Shaw, J. M. Dynamin assembly strategies and adaptor proteins in
403 mitochondrial fission. *Current biology : CB* **23**, R891-899, doi:10.1016/j.cub.2013.08.040
404 (2013).
405 36 Koirala, S. *et al.* Molecular architecture of a dynamin adaptor: implications for assembly
406 of mitochondrial fission complexes. *The Journal of cell biology* **191**, 1127-1139,
407 doi:10.1083/jcb.201005046 (2010).
408 37 Bleazard, W. *et al.* The dynamin-related GTPase Dnm1 regulates mitochondrial fission in
409 yeast. *Nature cell biology* **1**, 298-304, doi:10.1038/13014 (1999).
410 38 Osellame, L. D. *et al.* Cooperative and independent roles of the Drp1 adaptors Mff,
411 MiD49 and MiD51 in mitochondrial fission. *Journal of cell science* **129**, 2170-2181,
412 doi:10.1242/jcs.185165 (2016).
413 39 Palmer, C. S. *et al.* Adaptor proteins MiD49 and MiD51 can act independently of Mff and
414 Fis1 in Drp1 recruitment and are specific for mitochondrial fission. *J Biol Chem* **288**,
415 27584-27593, doi:10.1074/jbc.M113.479873 (2013).
416 40 Palmer, C. S. *et al.* MiD49 and MiD51, new components of the mitochondrial fission
417 machinery. *EMBO reports* **12**, 565-573, doi:10.1038/embor.2011.54 (2011).
418 41 Koirala, S. *et al.* Interchangeable adaptors regulate mitochondrial dynamin assembly for
419 membrane scission. *Proc Natl Acad Sci U S A* **110**, E1342-1351,
420 doi:10.1073/pnas.1300855110 (2013).
421 42 Frohlich, C. *et al.* Structural insights into oligomerization and mitochondrial remodelling
422 of dynamin 1-like protein. *Embo J* **32**, 1280-1292, doi:10.1038/emboj.2013.74 (2013).
423 43 Mears, J. A. *et al.* Conformational changes in Dnm1 support a contractile mechanism for
424 mitochondrial fission. *Nat Struct Mol Biol* **18**, 20-26, doi:10.1038/nsmb.1949 (2011).
425 44 Ingerman, E. *et al.* Dnm1 forms spirals that are structurally tailored to fit mitochondria.
426 *The Journal of cell biology* **170**, 1021-1027, doi:10.1083/jcb.200506078 (2005).
427 45 Ferguson, S. M. & De Camilli, P. Dynamin, a membrane-remodelling GTPase. *Nature*
428 *reviews. Molecular cell biology* **13**, 75-88, doi:10.1038/nrm3266 (2012).
429 46 Daumke, O. & Praefcke, G. J. Invited review: Mechanisms of GTP hydrolysis and
430 conformational transitions in the dynamin superfamily. *Biopolymers* **105**, 580-593,
431 doi:10.1002/bip.22855 (2016).
432 47 Lee, J. E., Westrate, L. M., Wu, H., Page, C. & Voeltz, G. K. Multiple dynamin family
433 members collaborate to drive mitochondrial division. *Nature* **540**, 139-143,
434 doi:10.1038/nature20555 (2016).
435 48 Loson, O. C., Song, Z., Chen, H. & Chan, D. C. Fis1, Mff, MiD49, and MiD51 mediate Drp1
436 recruitment in mitochondrial fission. *Molecular biology of the cell* **24**, 659-667,
437 doi:10.1091/mbc.E12-10-0721 (2013).
438 49 Faelber, K. *et al.* Crystal structure of nucleotide-free dynamin. *Nature* **477**, 556-560,
439 doi:10.1038/nature10369 (2011).
440 50 Ford, M. G., Jenni, S. & Nunnari, J. The crystal structure of dynamin. *Nature* **477**, 561-
441 566, doi:10.1038/nature10441 (2011).

51 Richter, V. *et al.* Structural and functional analysis of MiD51, a dynamin receptor required for mitochondrial fission. *The Journal of cell biology* **204**, 477-486, doi:10.1083/jcb.201311014 (2014).
52 Loson, O. C. *et al.* The mitochondrial fission receptor MiD51 requires ADP as a cofactor. *Structure* **22**, 367-377, doi:10.1016/j.str.2014.01.001 (2014).
53 Liu, R. & Chan, D. C. Drp1 recruitment by Mff, MiD51 and MiD49. *Molecular biology of the cell* **26** (2015).
54 Loson, O. C. *et al.* Crystal structure and functional analysis of MiD49, a receptor for the mitochondrial fission protein Drp1. *Protein Sci* **24**, 386-394, doi:10.1002/pro.2629 (2015).
55 Gao, S. *et al.* Structural basis of oligomerization in the stalk region of dynamin-like MxA. *Nature* **465**, 502-506, doi:10.1038/nature08972 (2010).
56 Haller, O., Gao, S., von der Malsburg, A., Daumke, O. & Kochs, G. Dynamin-like MxA GTPase: structural insights into oligomerization and implications for antiviral activity. *J Biol Chem* **285**, 28419-28424, doi:10.1074/jbc.R110.145839 (2010).
57 Reubold, T. F. *et al.* Crystal structure of the dynamin tetramer. *Nature* **525**, 404-408, doi:10.1038/nature14880 (2015).
58 Vanstone, J. R. *et al.* DNM1L-related mitochondrial fission defect presenting as refractory epilepsy. *Eur J Hum Genet* **24**, 1084-1088, doi:10.1038/ejhg.2015.243 (2016).
59 Sheffer, R. *et al.* Postnatal microcephaly and pain insensitivity due to a de novo heterozygous DNM1L mutation causing impaired mitochondrial fission and function. *Am J Med Genet A* **170**, 1603-1607, doi:10.1002/ajmg.a.37624 (2016).
60 Chang, C. R. *et al.* A lethal de novo mutation in the middle domain of the dynamin-related GTPase Drp1 impairs higher order assembly and mitochondrial division. *J Biol Chem* **285**, 32494-32503, doi:10.1074/jbc.M110.142430 (2010).
61 Gao, S., von der Malsburg, A., Haller, O., Kochs, G. & Daumke, O. Structural basis of oligomerization and the mechano-chemical function in dynamin-like MxA. *Faseb Journal* **25** (2011).
62 Antonny, B. *et al.* Membrane fission by dynamin: what we know and what we need to know. *Embo J* **35**, 2270-2284, doi:10.15252/embj.201694613 (2016).
63 Chappie, J. S. *et al.* A pseudoatomic model of the dynamin polymer identifies a hydrolysis-dependent powerstroke. *Cell* **147**, 209-222, doi:10.1016/j.cell.2011.09.003 (2011).
64 Mitchison, T. & Kirschner, M. Dynamic instability of microtubule growth. *Nature* **312**, 237-242 (1984).

Extended Data

Methods

Construct design

Wild type (WT) DRP1 isoform 2 sequence was purchased from DNASU (sequence ID HsCD00043627, UNIPROT identifier: O00429-3 also known as DLP1a) and was cloned into pET16b plasmid (Novagen) between the Nde1 and BamH1 sites. The vector was kindly provided by the laboratory of Wesley I. Sundquist with a 10X-His tag followed by a PreScission protease site (Leu-Glu-Val-Leu-Phe-Gln-Gly-Pro). Wild-type $MID49_{126-454}$ sequence was PCR amplified and cloned into pGEX6p1 vector having an N-terminal GST tag followed by a PreScission protease site. Site directed mutagenesis was performed on pET16b-DRP1 using the Gibson cloning method to introduce mutations[1]. All constructs were verified using Sanger sequencing.

Protein purification

Protein purification was performed as described[2]. Briefly, plasmids containing the WT DRP1 or $MID49_{126-454}$ sequence were transformed in the BL21-DE3 (RIPL) strain of *E. coli*. The colonies were inoculated in LB culture medium and grown overnight. Secondary inoculations were done the next morning in ZY medium for auto-induction[3,4]. The cultures were grown to an OD_{600} of 0.8 at 37°C in baffled flasks and were shifted to 19°C to grow for another 12 hours. The cultures were spun down and the bacterial pellets were used for protein purification immediately or stored at -80°C.

Full length DRP1 WT and mutant variants were purified as described previously for DRP1 WT with modifications[5]. Briefly, the bacterial pellets were resuspended in buffer A (50 mM

HEPES/NaOH (pH 7.5), 400 mM NaCl, 5 mM $MgCl_2$, 40 mM imidazole, 1 mM DTT, 0.5 mg DNase (Roche) and protease inhibitors (10 mM pepstatin, 50 mM PMSF, 0.5 mM aprotinin and 2 mM leupeptin), followed by cell disruption with a probe sonicator. Lysates were cleared by centrifugation at 40,000xg in Beckman JA 25.5 rotors for 60 min at 4°C. The supernatant was filtered using a 0.45 μm filter and applied to Ni-NTA Agarose beads pre- equilibrated with buffer B (50 mM HEPES/NaOH (pH 7.5), 400 mM NaCl, 5 mM $MgCl_2$, 40 mM imidazole, 1 mM DTT). The beads were washed with 20 column volumes each of buffer B and buffer C (50 mM HEPES/NaOH (pH 7.5), 800 mM NaCl, 5 mM $MgCl_2$, 40 mM imidazole, 1 mM DTT, 1 mM ATP, 10 mM KCl) followed by buffer D (50 mM HEPES/NaOH (pH 7.5), 400 mM NaCl, 5 mM $MgCl_2$, 80 mM imidazole, 1 mM DTT, 0.5% (w/v) CHAPS). A final pre-elution wash was done with 20 column volumes of buffer B. Bound DRP1 was eluted with buffer E (50 mM HEPES/NaOH (pH 7.5), 400 mM NaCl, 5 mM $MgCl_2$, 300 mM imidazole, 1 mM DTT) and dialyzed overnight at 4°C against buffer B without imidazole in the presence of PreScission protease to cleave the N-terminal 10X-His tag. The protein was re-applied to a Ni-NTA column pre-equilibrated with dialysis buffer and was observed to bind the column without the 10X-His tag as well. Subsequently, the protein was eluted with buffer B containing 80 mM imidazole.

Pure protein was concentrated with a 30kDa molecular weight cutoff (MWCO) centrifugal concentration device (Millipore). In a final step, DRP1 was purified by size-exclusion chromatography (SEC) on a Superdex-200 column (GE) in buffer F containing 20 mM HEPES/ NaOH (pH 7.5), 300 mM NaCl, 2.5 mM $MgCl_2$ and 1 mM DTT. Fractions containing DRP1 were pooled, concentrated, flash frozen as single use aliquots in liquid nitrogen and stored at -80°C. Exact masses for purified DRP1 proteins were validated by MALDI-TOF mass spectrometry.

$MID49_{126-454}$ was purified as described with modifications[6]. pGEX6p1-$MID49_{126-454}$ plasmid DNA (human, UNIPROT identifier: Isoform 1 Q96C03-1, also known as MIEF2) was transformed in BL21 (DE3) RIPL cells. The colonies were grown overnight in LB medium and secondary cultures were grown in ZY medium. Cells were grown to an OD_{600} of 0.8-1, collected by centrifugation and processed immediately or stored at -80°C as described above. The bacterial pellets were lysed as described above in MID-buffer A (50 mM Tris pH 8.0, 500 mM NaCl, 5% glycerol, 1 mM DTT and 0.1% (v/v) Triton X-100). The lysates were pre-cleared at 40,000xg and filtered using a 0.45 μm filter before applying to 3 ml glutathione sepharose beads (GE). After overnight binding to beads, the unbound protein was removed and the beads were washed using 20 column volumes each of MID-buffer A and MID-buffer B (50 mM Tris pH 8.0, 500 mM NaCl, 5% glycerol, 1 mM DTT). The protein was eluted with MID-buffer C (50 mM Tris pH 8.0, 500 mM NaCl, 5% glycerol, 1 mM DTT and 20 mM reduced glutathione). The eluate was cleaved overnight with PreScission protease while dialyzing against MID-buffer D (20 mM Tris pH 8.0, 100 mM NaCl, 5% glycerol, 1 mM DTT). Cleaved protein was further purified using ion-exchange chromatography using a Q sepharose (GE) column. The low salt buffer for ion-exchange was the same as MID-buffer D and the high salt buffer was MID-buffer E (20 mM Tris pH 8.0, 1 M NaCl, 5% glycerol, 1 mM DTT). The relevant $MID49_{126-454}$ fractions were pooled, concentrated and further purified using an SEC column pre-equilibrated with MID-buffer F (20 mM Tris pH 8.0, 200 mM NaCl, 5% glycerol, 1 mM DTT). The fractions containing $MID49_{126-454}$ were pooled, concentrated, flash frozen in liquid nitrogen and stored as single use aliquots at -80°C.

Filament assembly, EM sample preparation, data acquisition and processing

To assemble DRP1-$MID49_{126-454}$ filaments, the proteins were mixed to a final concentration of 2 μM each and kept for an hour at room temperature. The mixture was dialyzed against assembly

buffer (20 mM HEPES pH 7.5, 50 mM KCl, 3 mM $MgCl_2$, 1 mM DTT, 200 μM GMPPCP and the detergent octyl-glucopyranoside (Anatrace) at 0.2% final concentration). The filaments were observed by screening in negative stain or vitrified for cryo-EM. For vitrification, the sample was applied to Quantifoil holey carbon grids (R2/2) using a Vitrobot Mark III with 3.5 μl sample, 5 seconds blotting time and a 0 mm offset at 19°C and 100% humidity. Images were collected on an FEI T30 Polara operating at 300kV at a magnification of 31000X. Images were recorded on a Gatan K2 summit camera in super resolution mode that had a binned pixel size of 1.22 Å/pixel. The images were dose fractionated, containing 30-40 frames with a total exposure time of 6-8 seconds, 0.2 seconds per frame and a per frame dose of 1.42 electrons/$Å^2$. SerialEM was used to automate data collection[7]. The defocus range was 0.8-3 μm under focus. The data was motion corrected and dose-weighted using UCSF Motioncorr2[8]. CTF parameter estimation on the non-dose-weighted but motion-corrected stacks was done using CTFFIND4 and GCTF[9,10].

Filaments were boxed using the program e2helixboxer.py from the EMAN2 suite[11]. Particle coordinates were used to extract discrete particles using RELION 1.3-1.4[12] and all further processing was done within the RELION suite. Multiple rounds of 2D classification identified the most well-ordered segments, and 3D autorefine was run using a Relion1.2 version with the IHRSR algorithm implemented[13,14]. The consensus helical structure was used to classify the particles without refining helical symmetry (using RELION 1.4), resulting in 2 major classes that differed slightly in rise and twist (Extended data figure 4). Particles from each class were selected and independently refined again with helical RELION 1.2 and IHRSR. Analysis of these reconstructions revealed that each structure was comprised of three linear filaments that bundle together to form a structure that resembled a triangle in cross-section (Extended data figures 3-4). The vertices of the triangle are formed through asymmetric interactions between the G-domains in adjacent filaments. The significance of these asymmetric G domain interactions has

not been evaluated. The triangular arrangement of the bundled helices is unlikely to correspond to a biologically meaningful architecture, and this structure cannot form if the MID49 receptor is embedded in the outer mitochondrial membrane.

To further improve signal-to-noise, each of the three filaments in each independent half-map was segmented, extracted, resampled on a common grid and summed using UCSF Chimera[15-19]. The respective symmetrized but unfiltered half maps from each class were again aligned to a common grid, summed, averaged along the C2 symmetry axis of the DRP1 dimer. In a last step, relion_postprocess was used to add the resulting and fully symmetrized half maps (Extended data figure 4). These half maps and the final summed map, with differential B-factor sharpening per region (Extended data figures 4-9), were used for atomic modeling using Rosetta as described below.

For the projection structure of the $DRP1_{G362D}$ rings, 2 μM protein was mixed 1:1 molar ratio with $MID49_{126-454}$ and was allowed to sit at room temperature for an hour. The mixture was dialyzed against the assembly buffer (without detergent) overnight. The sample was collected after 12 hours and vitrified using ultra-thin 3 nm carbon support films (Ted Pella). For vitrification, a Mark III vitrobot was used with 3.5 μl sample, 0 mm offset, 100% humidity and 3.5 seconds blot time. The images were collected using an FEI TF20 microscope and SerialEM for automated data collection. The data were recorded with a Gatan K2 camera operating in super resolution mode to collect dose fractionated movie stacks using a binned pixel size of 1.234 Å/pixel. 40 frames were collected per stack (0.2 seconds per frame and 1.42 electrons/$Å^2$). The movie stacks were motion corrected and the parameters of the transfer function were estimated as described above. Approximately 2000 particles were picked manually for initial 2D classification in RELION 1.4 and these averages were used as templates for further particle picking by

Gautomatch (http://www.mrc-lmb.cam.ac.uk/kzhang/). Final 2D averaging of the entire rings versus quarter segments of the rings were computed using Relion1.4.

Model building

The general procedure for atomic model interpretation and validation using Rosetta were performed as described[20]. To obtain an initial model for DRP1, the crystal structure of nucleotide-free DRP1 (PDB ID: 4BEJ)[5] was used for the stalk region and DRP1 G domain-BSE structures bound to GMPPCP (PDB ID: 3W6O) were used for the G-domain and BSE regions. Density-guided model completion for DRP1 was carried out with RosettaCM[21] using this hybridization of DRP1 crystal structures. A converged solution appeared from the low-energy ensemble of the complete models generated by RosettaCM. However, among the low-energy ensemble, residues 503-612 were found to be extremely flexible without cryoEM density constraints and therefore were omitted for further coordinate refinement. For MID49, the highly homologous mouse MID49 crystal structure (81.3% identity, PDB ID: 4WOY, Extended Data Fig. 7)[6] was used to generate a homology model using RosettaCM and used as the starting model.

To enable fragment-based, density-guided model refinement with missing residues (503-612, DRP1), Rosetta iterative local rebuilding tool was customized to disallow backbone rebuilding at breaks within a single chain. Multiple rounds of refinement were done for each component against one half map (training map), and the other half map (validation map) was used to monitor overfitting according to the detailed procedure described in Wang et al.[20].

With the refined model of DRP1 and MID49, we further refined the model in the context of a full assembly that included 8 identical copies of each protein, Mg^{2+} and nucleotide which included all possible inter-domain molecular interactions in the filament (Extended data figure 8).

Pseudo-symmetry was used[22] to enable and facilitate the energy evaluations of all neighboring interactions around the asymmetric unit (Green model, shown in Extended data figure 8) for final model refinement of the full assembly. To this end, refinement was done against the training map. Finally, the half maps were used to determine a weight for the density map that did not introduce overfitting. Using the weight and with the symmetry imposed, the whole assembly of DRP1 and MID49 was refined in the full map, followed by B-factors refinement[23]. Finally, quantification of buried surface area and the number and nature of the bonds involved for each DRP1-MID49 interaction interface modeled by Rosetta were performed with the PISA server (http://www.ebi.ac.uk/pdbe/pisa/).

To design a molecular model for the closed 12-dimer DRP1 rings, we used the diameter, thickness, and angles revealed by the 2D cryoEM class averages of the $DRP1_{G362D}$ rings stabilized with GMPPCP. The atomic coordinates determined above using RosettaCM were used to build the ring in sections, first with repeating dimers of the interface-2 “X-shaped” stalk, then the BSE and finally the G-domains and the angles between these sections were iteratively adjusted until calculated projections of the molecular model corresponded with the features of the experimental projection densities. Both the top (Fig 4b-c) and the side view (Extended data Figure 15) were used as constraints. The complete atomic model of ring was finally refined in Phenix[24] to minimize clashes.

Extended data Table 1

Data Collection	Filaments	Ring
Particles	412684	61574
Pixel Size (Å)	1.22	1.234
Defocus Range (microns)	0.3-4.0	0.3-5.0
Defocus Mean (microns)	1.3	2.1
Defocus Median (microns)	1.3	2.08
Voltage (kV)	300	200
Per frame electron dose ($e^{/}Å^2$)	1.42	1.42
Refinement		
Resolution	4.2 Å ($FSC_{average}$)	6.1 Å (FRC)
Map sharpening B-factor	-225 (average)	
DRP1 stalk only	-300 to -400	
MID49 only	-150 to -200	
G-domain & BSE	-200	
Validation		
Molprobity score	1.41	1.84
Clashscore, all atoms	2.13	4.94
Favored rotamers (%)	99.25	99.44
RMS (bonds)	0.0107	0.011
RMS (angles)	0.97	1.62
Ramachandran Statistics		
Favored (%)	93.6	88.9
Outliers (%)	1.32	0.37

Extended data figures

Kalia, et al.
Extended Data Fig. 1

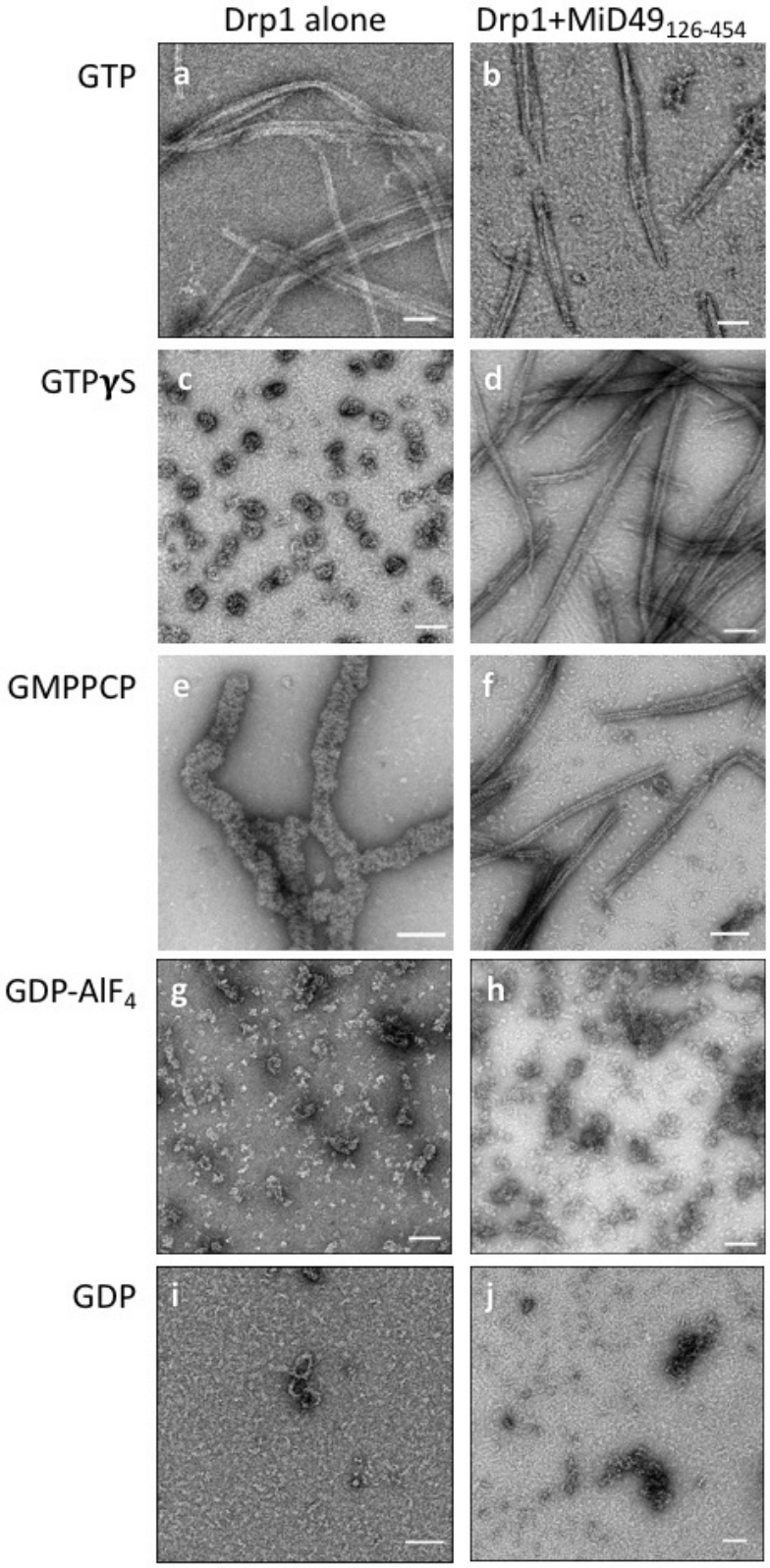

Extended data figure 1: DRP1 assembly states visualized with negative stain electron microscopy in the presence of different guanine nucleotides and stoichiometric $MID49_{126-454}$ ([2μM] for both proteins). Bars = 100nm.

Kalia, et al.
Extended Data Fig. 2

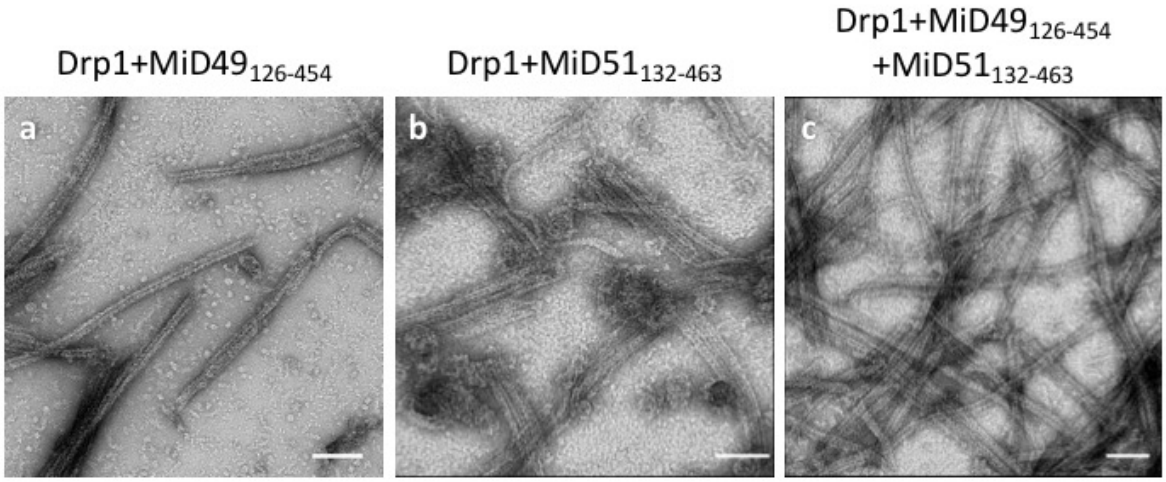

Extended data figure 2: $MID49_{126-454}$ and $MID51_{132-463}$ form indistinguishable assemblies with DRP1 by negative stain electron microscopy. **(a)** DRP1 plus $MID49_{126-454}$ and GMPPCP; **(b)** DRP1 plus $MID51_{132-463}$ and GMPPCP, **(c)** DRP1 plus both MID49 and MID51. Bars = 100nm.

Kalia, et al.
Extended Data Fig. 3

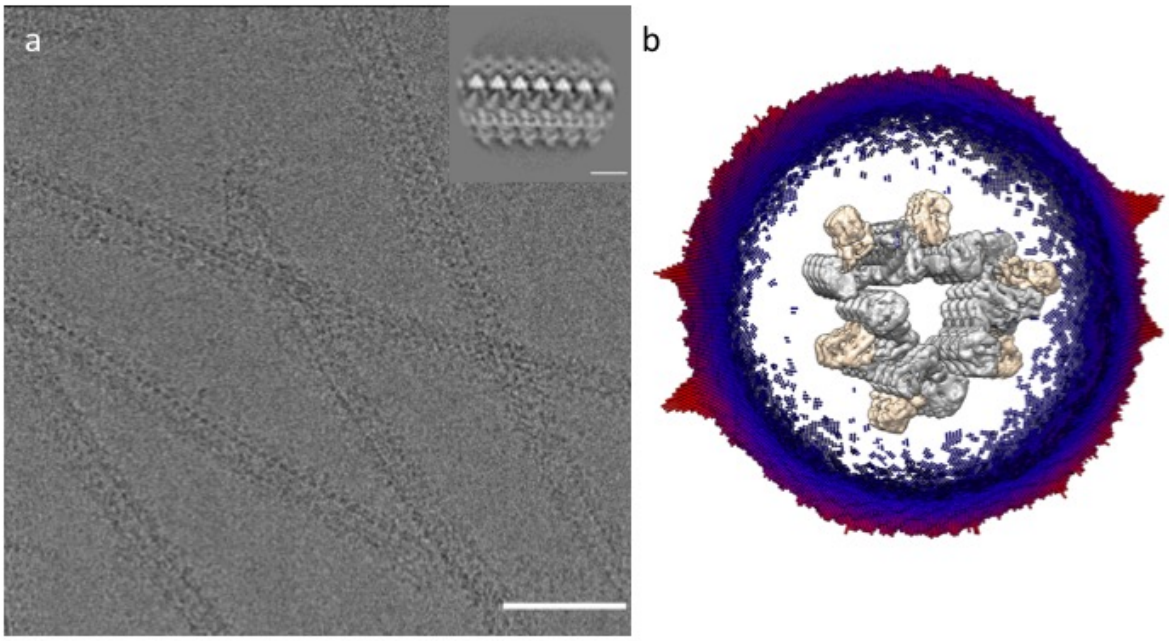

Extended data figure 3: CryoEM imaging and reconstruction. **(a)** An electron cryo-micrograph of DRP1-MID49$_{126-454}$ filaments formed with GMPPCP. Inset shows a representative 2D class average. Bar =100nm, Inset bar =10nm. **(b)** Oblique cross-section of the 3D reconstruction and the distribution of views determined during helical reconstruction. DRP1 density is rendered in grey, MID49 in golden yellow.

Kalia, et al.
Extended Data Fig. 4

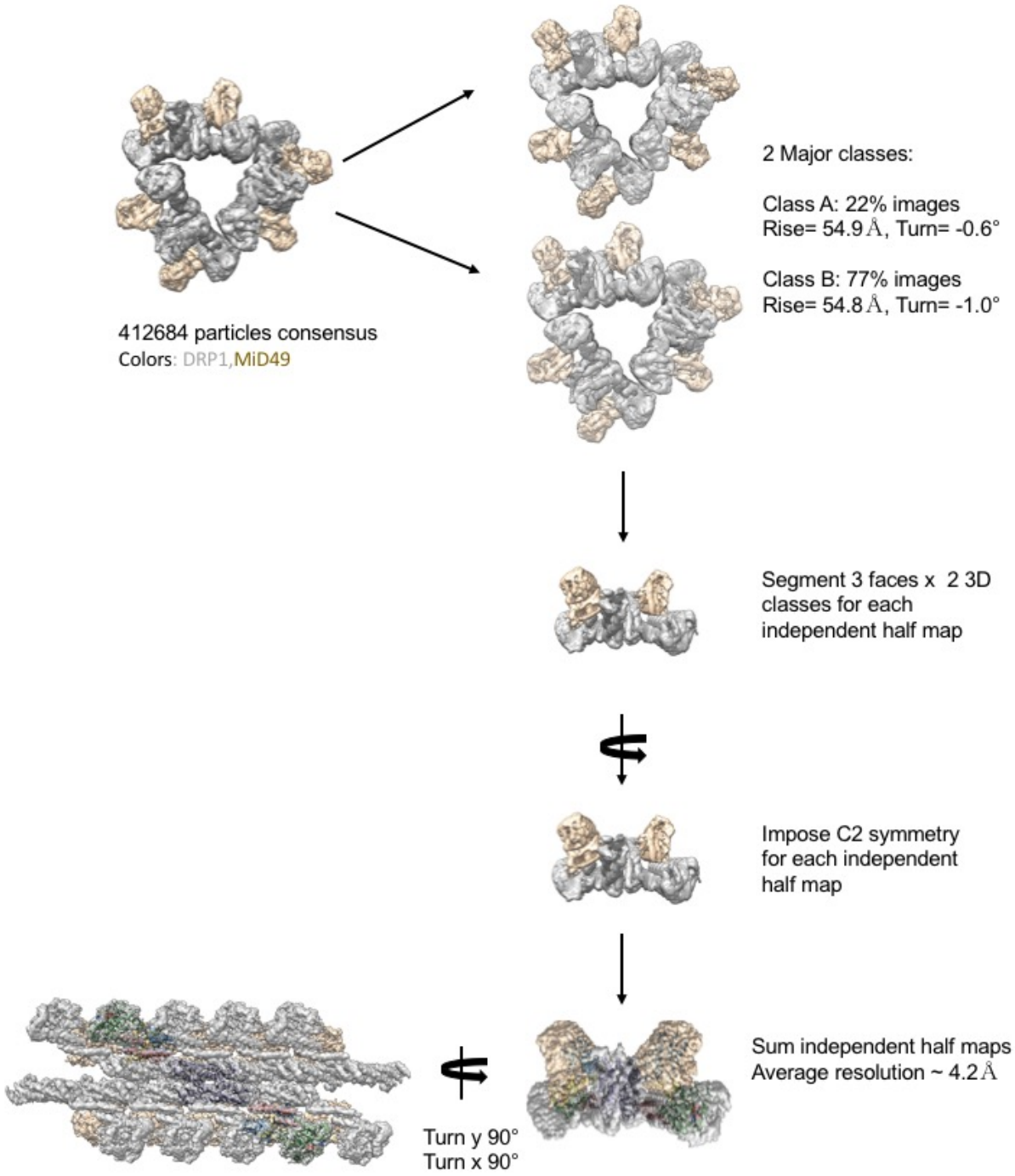

Extended data figure 4: Raw particle numbers and workflow for the reconstruction protocol and imposition of symmetries. DRP1 density is rendered in grey, MID49 in golden yellow.

Kalia, et al.
Extended Data Fig. 5

a

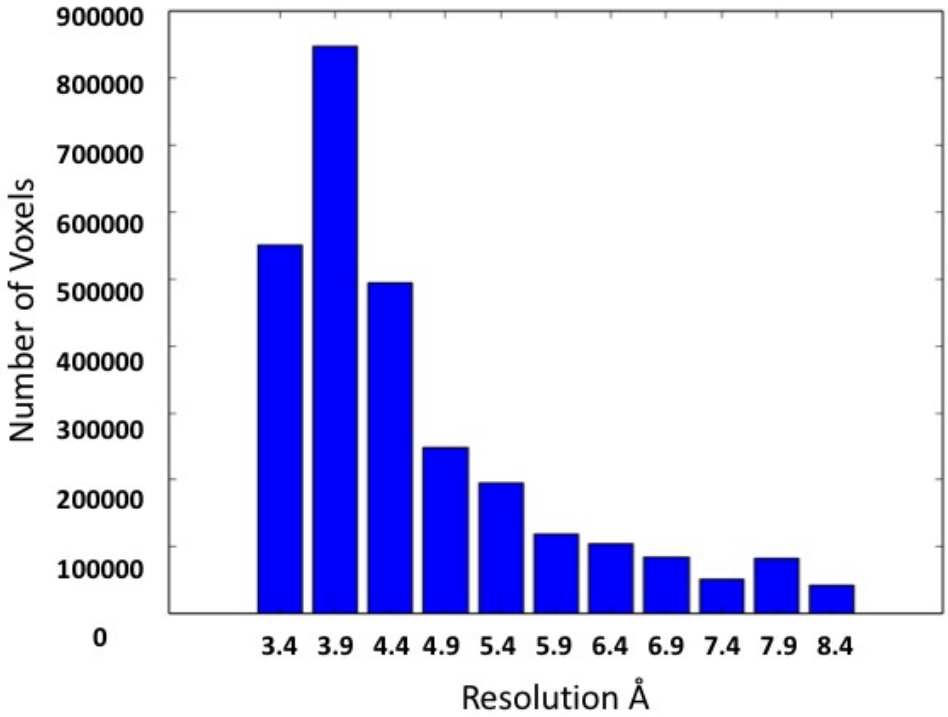

b

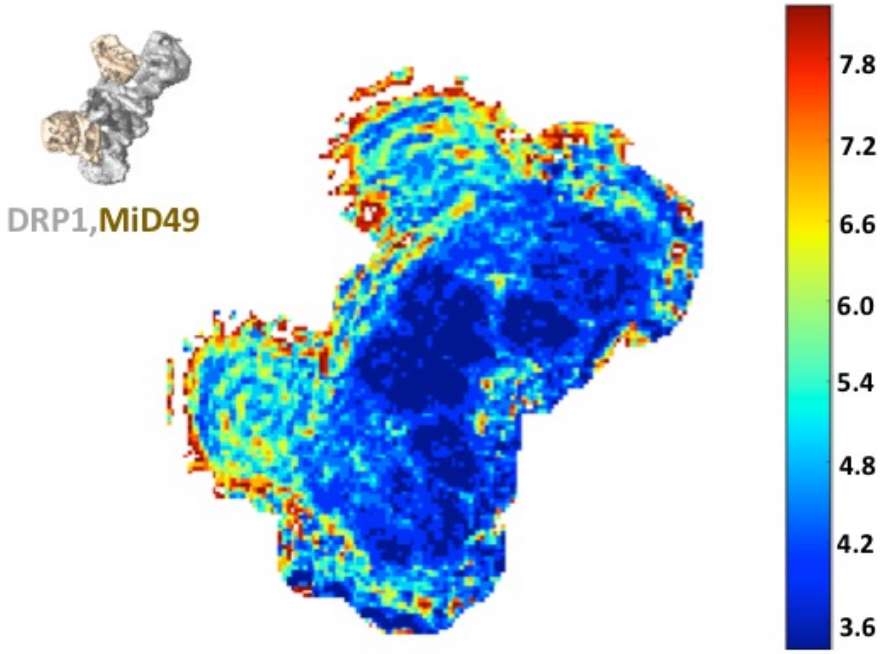

Extended data figure 5: Local resolution estimates computed by Resmap[25]. **(a)** Histogram of voxels values, and **(b)** Heat map of local resolution estimates displayed for a cross-section through the reconstruction.

Kalia, et al.
Extended Data Fig. 6

a

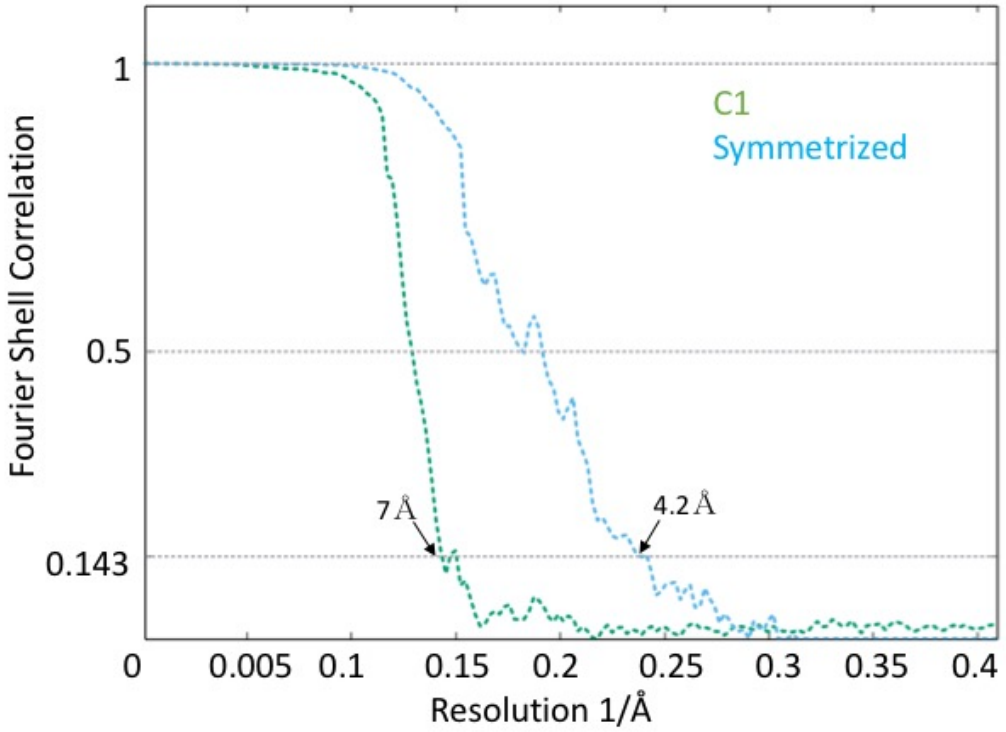

b

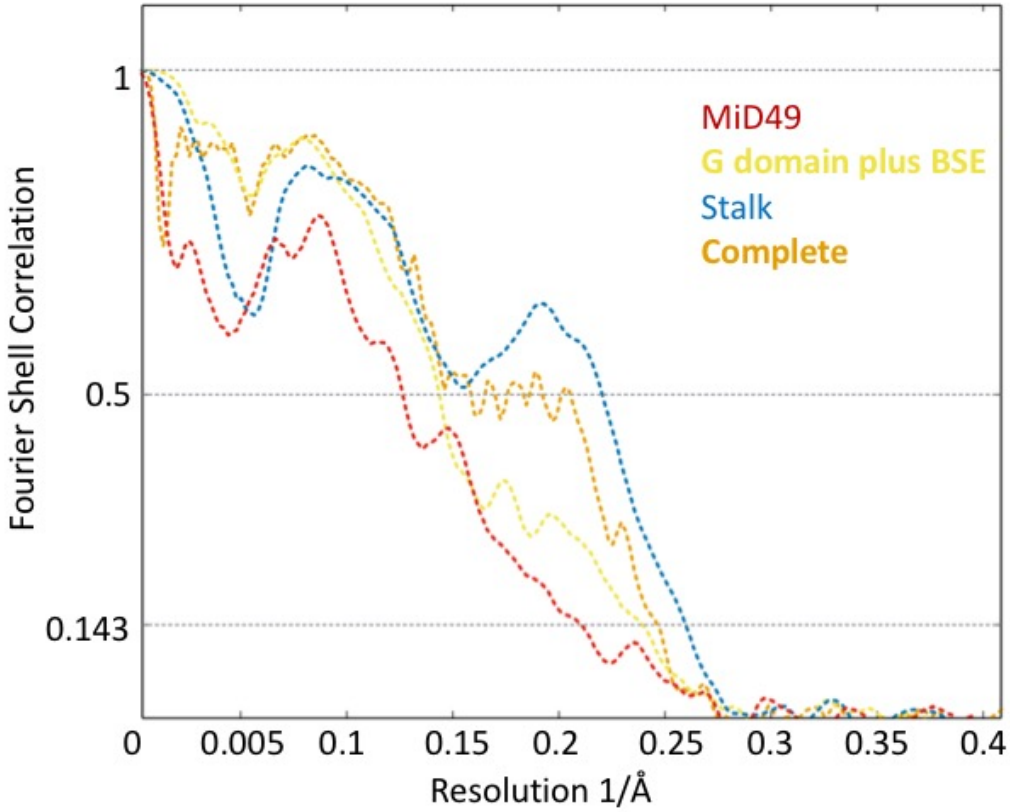

Extended data figure 6: Fourier Shell Correlation plots for **(a)** the half-maps with and without imposed symmetry; and **(b)** model-to-map correlations for the averaged as well as each sub-region of the structure using the atomic coordinates and B-factors determined using Rosetta.

Kalia, et al.
Extended Data Fig. 7

a

```
                 1         10        20        30        40        50        60
MiD49_Mouse      MAEFSQKQRKQSGSEGLGSVVDFLLANARLVLGVGGAAVLGIATLAVKRLIDRATSPPDE
MiD49_Human      MAEFSQKRGKRRSDEGLGSMVDFLLANARLVLGVGGAAVLGIATLAVKRFIDRATSPRDE

                        70        80        90       100       110       120
MiD49_Mouse      DDTKGDSWKELSLLRATSPQKPQPPPAAFSQPLATGSPSPSVPVEPTPIHSPTTPKFSTI
MiD49_Human      DDTKADSWKELSLLKATPHLQPRPPPAALSQPVLPLAPSSSAPEGPAETDPEVTPQLSSP

                       130       140       150       160       170       180
MiD49_Mouse      APLCLTFQERLLAFERKHVITPEAHVTLAKQLAGDIALELQAYLRSKFPELPFGALVPGG
MiD49_Human      APLCLTLQERLLAFERDRVTIPAAQVALAKQLAGDIALELQAYFRSKFPELPFGAFVPGG

                       190       200       210       220       230       240
MiD49_Mouse      PLYDGLQAGTAEHVRLLAPLELEPGLWSLVPGVDTVAREPRCWAVRRTQLEFHPRGCSPW
MiD49_Human      PLYDGLQAGAADHVRLLVPLVLEPGLWSLVPGVDTVARDPRCWAVRRTQLEFCPRGSSPW

                       250       260       270       280       290       300
MiD49_Mouse      DRFLVGGYLSSRVLLELLRKALSASVNWPAIGSLLGCLIWPDVASEELLLKVQHECLEFT
MiD49_Human      DRFLVGGYLSSRVLLELLRKALAASVNWPAIGSLLGCLIRPSMASEELLLEVQHERLELT

                       310       320       330       340       350       360
MiD49_Mouse      LAVLMVVPGASTDDRLLLAWPLEGLASNLWLQDLYPVETARLRALDDQDAGTRRRLLLLL
MiD49_Human      VAVLVAVPGVDADDRLLLAWPLEGLAGNLWLQDLYPVEAARLRALDDHDAGTRRRLLLLL

                       370       380       390       400       410       420
MiD49_Mouse      CGICRGHPALVRLGWSHLTQVVLHLGEEEVAWTEEALGERFLQALEFLVGSLEQASLPCH
MiD49_Human      CAVCRGCSALGQLGRGHLTQVVLRLGEDNVDWTEEALGERFLQALELLIGSLEQASLPCH

                       430       440       450
MiD49_Mouse      FNPSVNLLGNFREEEIDDIGYVLYSGLQVPESLF
MiD49_Human      FNPSVNLFSSLREEEIDDIGYALYSGLQEPEGLL
```

b

MiD49 human (this study)
MiD49 mouse (PDB:4WOY)

Extended data figure 7: Modeling of human MID49. **(a)** Sequence alignment between human and mouse MID49 sequences. **(b)** Overlay of the homology model of human $MID49_{126-454}$ (blue, with yellow DRR, ribbon) modeled within the cryoEM density versus the mouse MID49 crystal structure (PDB ID: 4WOY, grey ribbon)[6].

Kalia, et al.
Extended Data Fig. 8

a

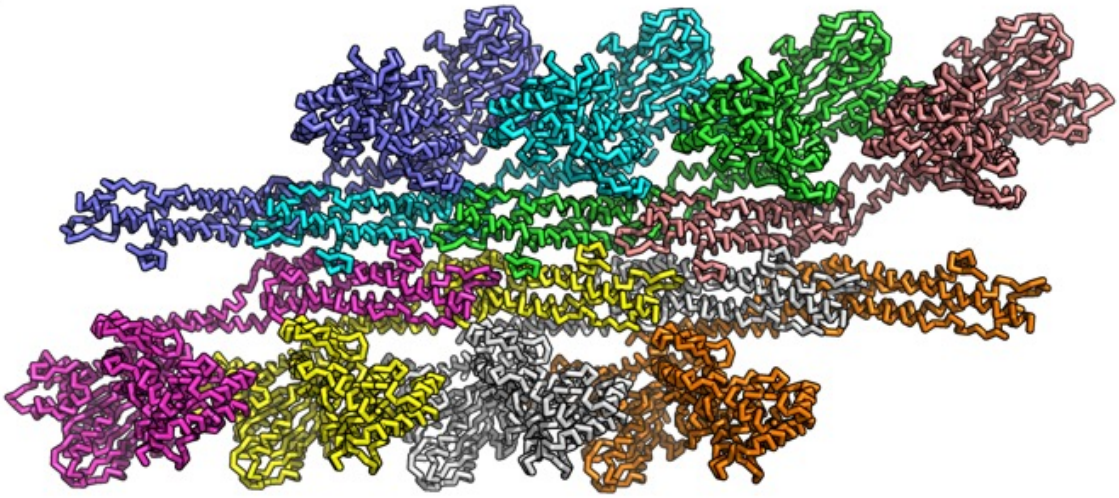

b

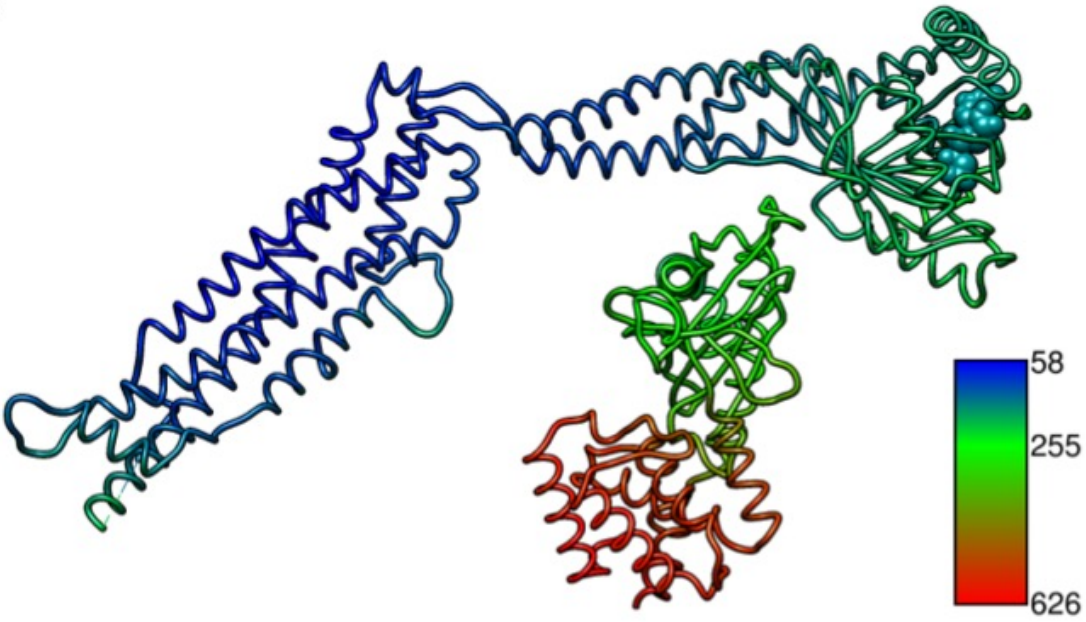

Extended data figure 8: Rosetta refinement. **(a)** Symmetric unit of the filament with 8 chains of DRP1 and 8 chains of MID49 refined using Rosetta to enforce symmetry and account for all possible inter-molecular interfaces. **(b)** Atomic B-factors for the DRP1 and MID49 models (ribbon) and bound GMPPCP (space filling).

Kalia, et al.
Extended Data Fig. 9

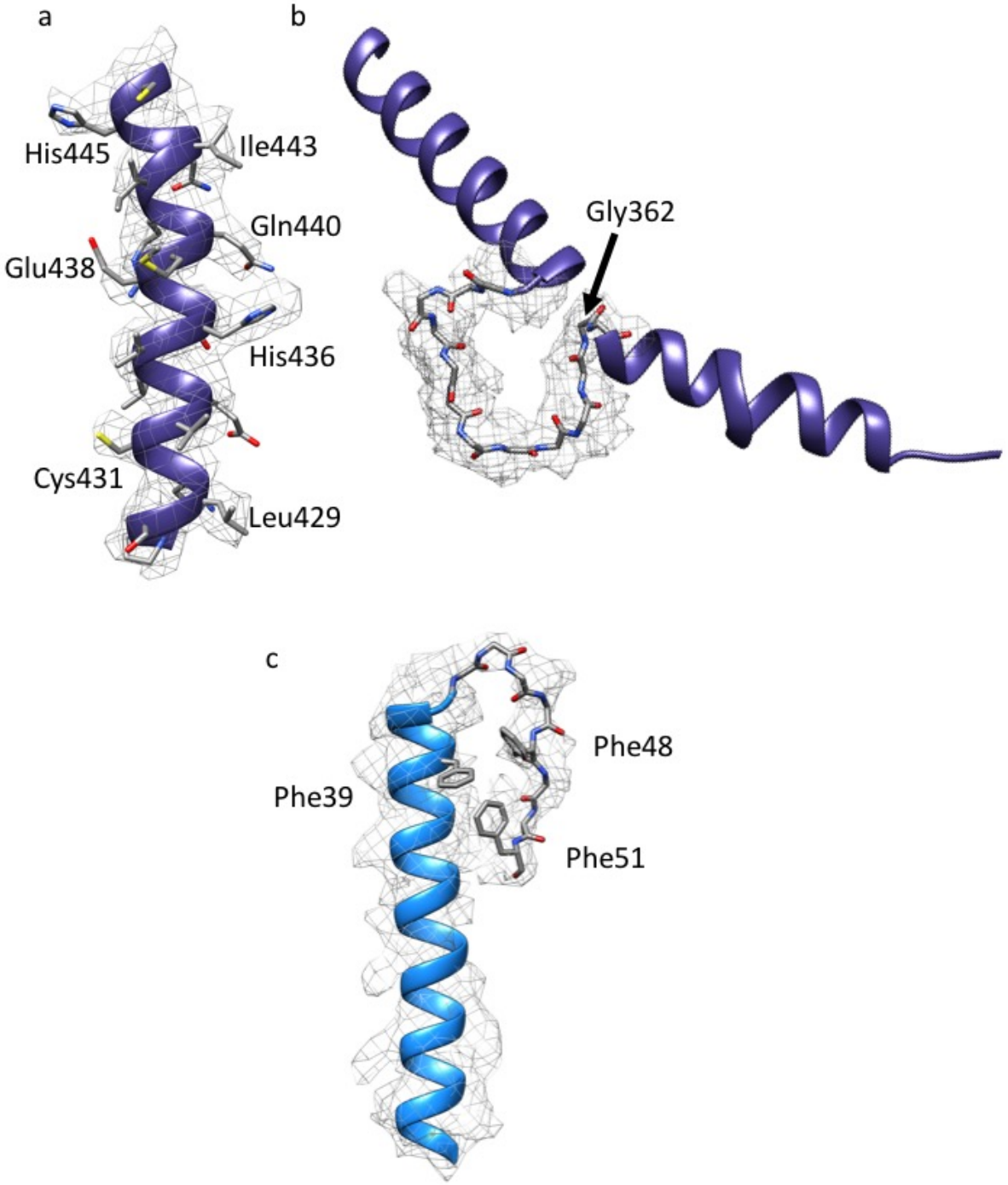

Extended data figure 9: Examples of model fitting to B-factor sharpened density for **(a)** a helix from the DRP1 stalk, **(b)** the backbone of the L1N^{S} loop, and **(c)** a helix and loop from MID49.

Kalia, et al.
Extended Data Fig. 10

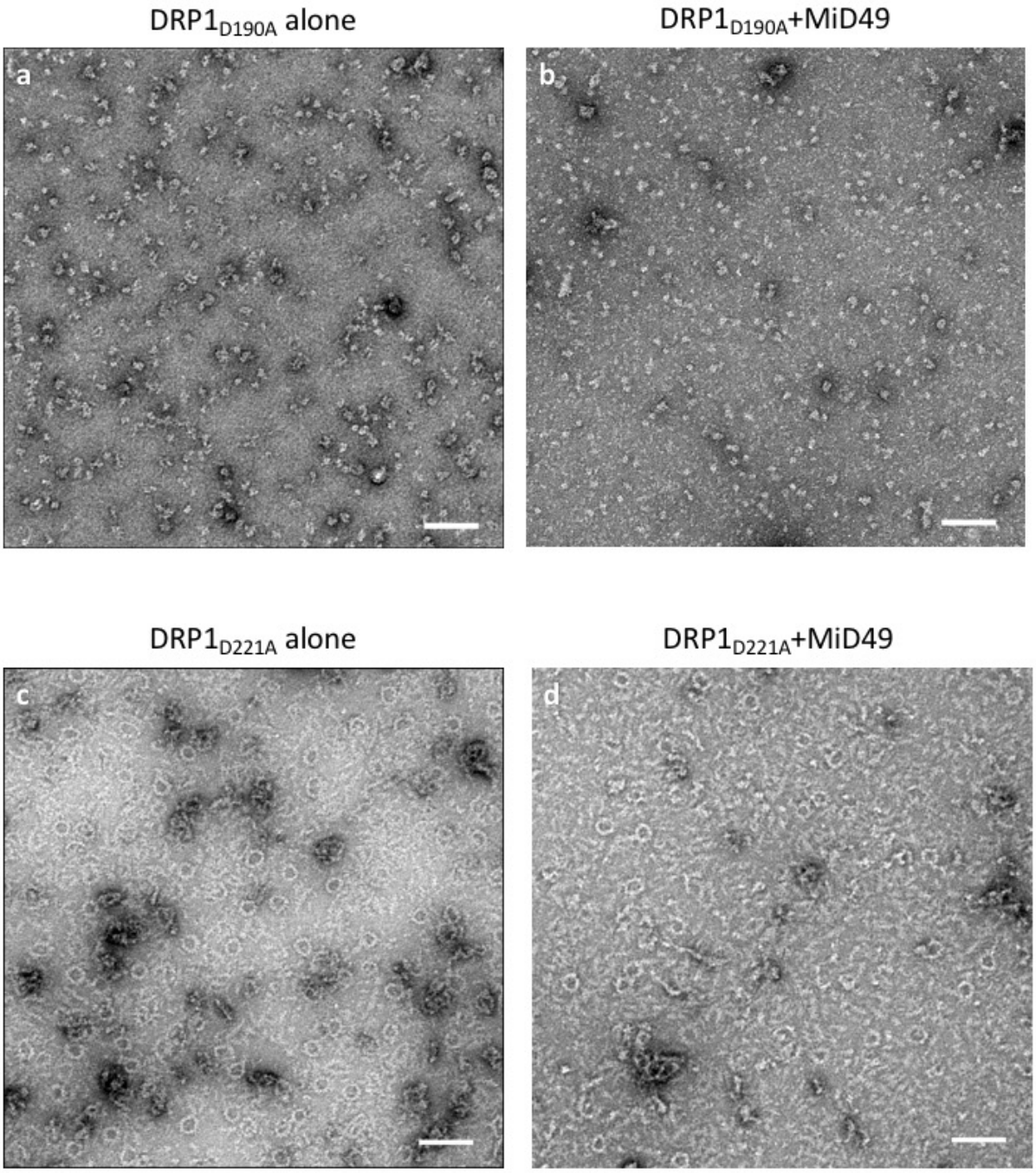

Extended data figure 10: DRP1 assembly and coassembly reactions with GMPPCP for **(a)** $DRP1_{D190A}$ alone, **(b)** $DRP1_{D190A}$+MID49, **(c)** $DRP1_{D221A}$ alone, and **(d)** $DRP1_{D221A}$+MID49. Bars = 100nm.

Kalia, et al.
Extended Data Fig. 11

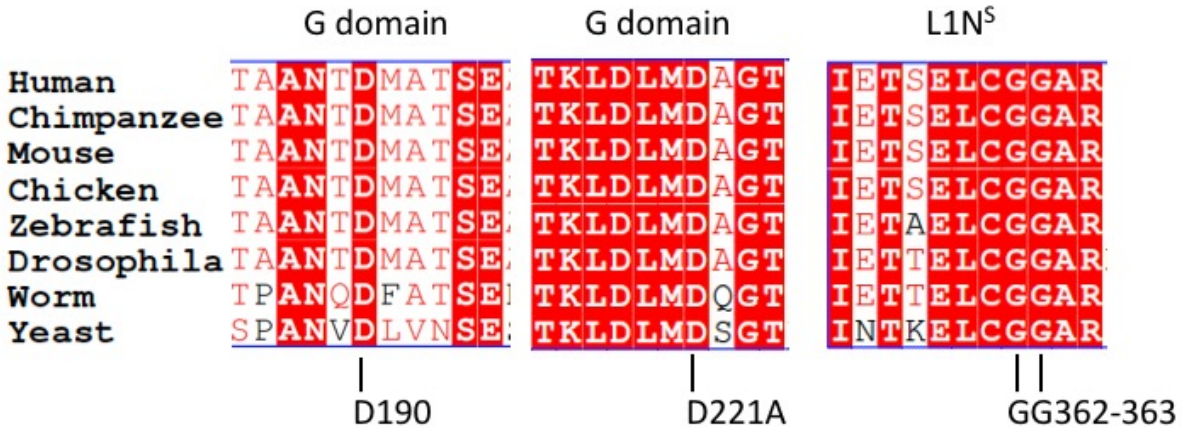

Extended data figure 11: Multiple sequence alignment of the regions near and including the DRP1 residues mutated in this study: D190, D221 and G362. The residue numbers apply to human DRP1, isoform 2 (UNIPROT identifier: O00429-3 also known as DLP1a).

Kalia, et al.
Extended Data Fig. 12

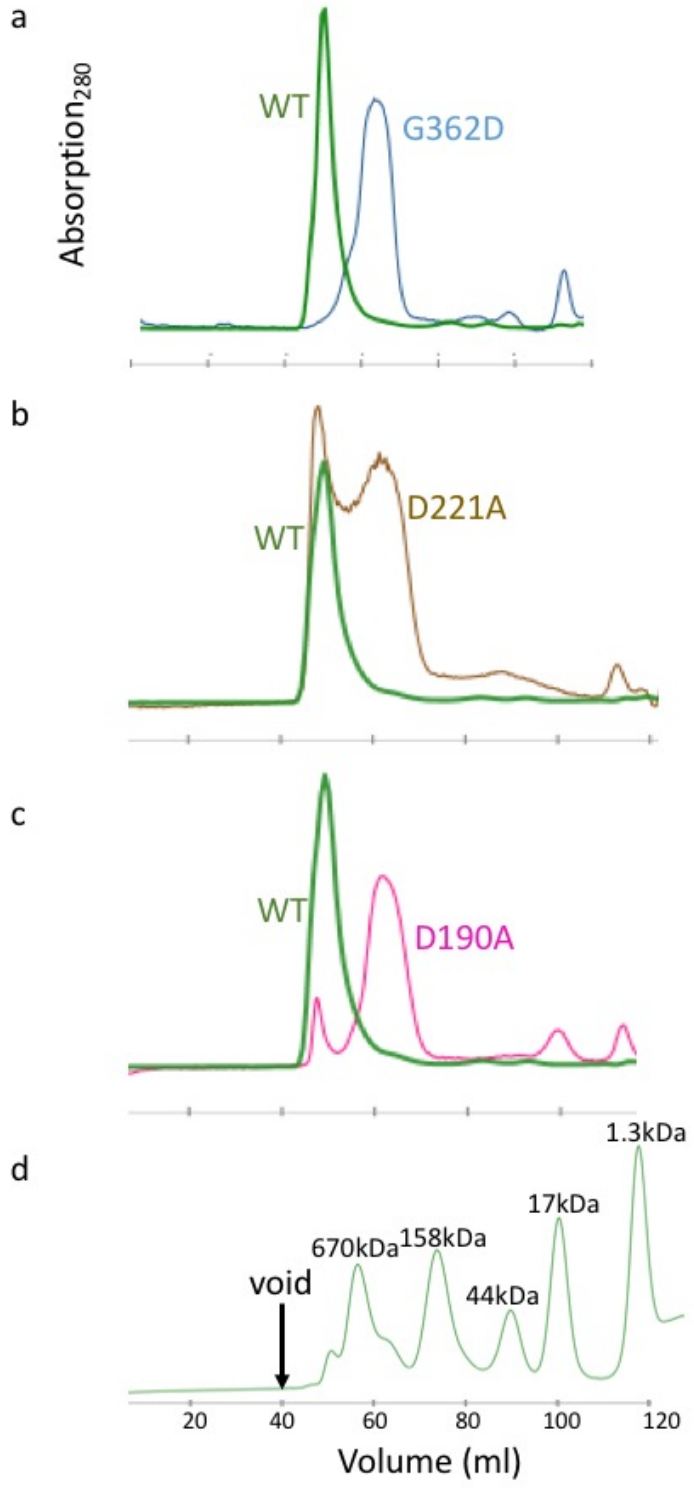

Extended data figure 12: Size exclusion chromatography traces for DRP1 wild-type and mutants used in the study. **(a)** Comparison between wild type (WT) versus $DRP1_{G362D}$, **(b)** WT versus $DRP1_{D221A}$, and **(c)** WT versus $DRP1_{D190A}$. **(d)** Standards for molecular weight comparison.

Kalia, et al.
Extended Data Fig. 13

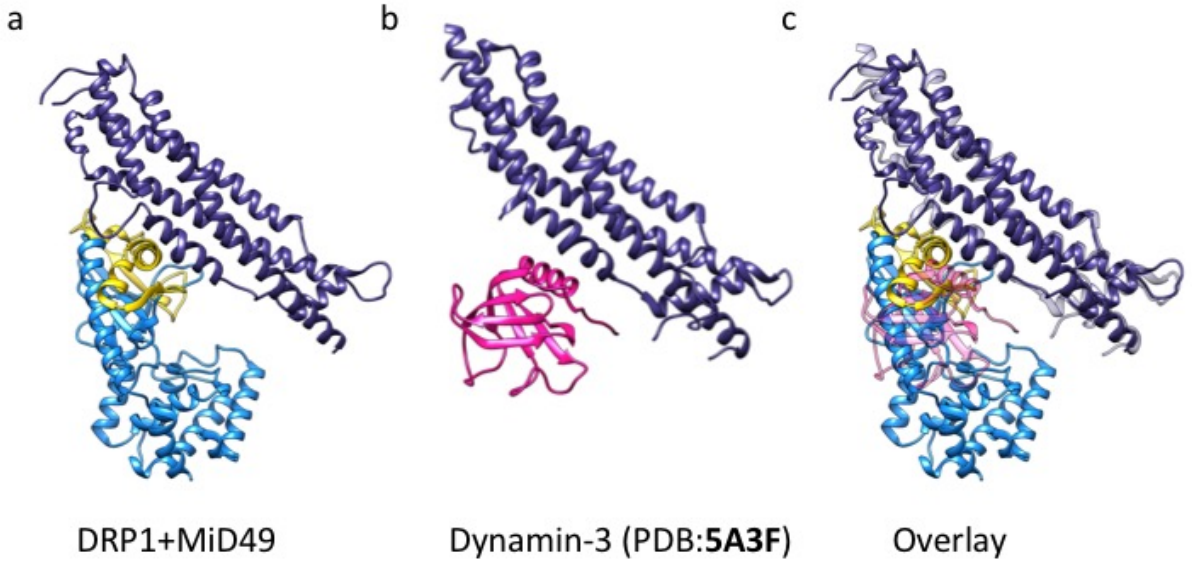

Extended data figure 13: Structural similarities between the third DRP1-MID49 interaction interface that includes the L1N^{S} loop and the interaction between the Pleckstrin Homology (PH) domain and the stalk of Dynamin-3 (PDB ID:5A3F)[26]. **(a)** DRP1-MID49 interaction at MID-interaction interface 3, **(b)** the PH domain bound to the stalk of Dynamin-3, and **(c)** Overlay of a and b.

Kalia, et al.
Extended Data Fig. 14

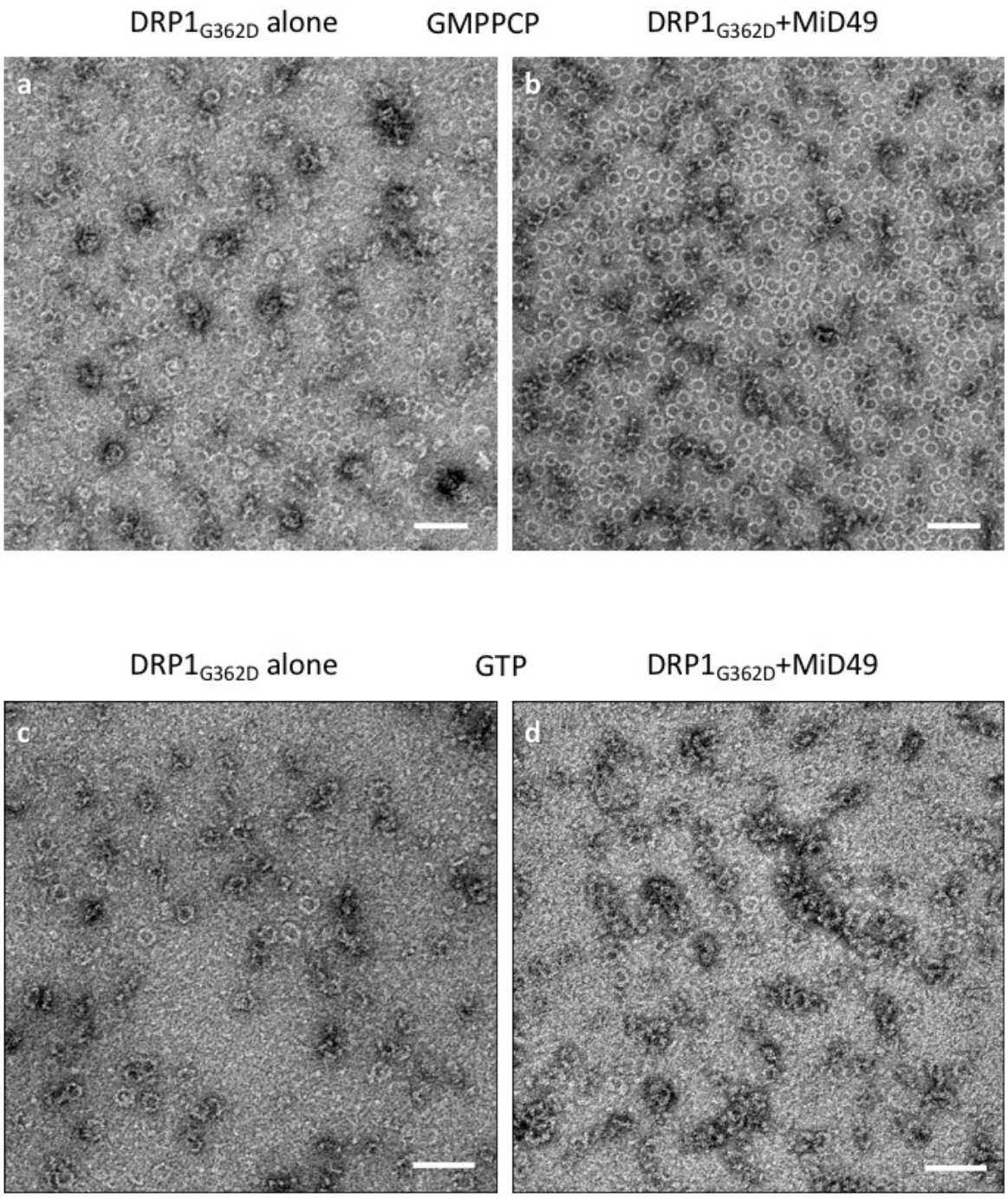

Extended data figure 14: $DRP1_{G362D}$ assembly and coassembly reactions with GMPPCP or GTP. $DRP1_{G362D}$ forms rings but not linear filaments without MID49 **(a,c)**; and with MID49 present **(b,d)**; with GMPPCP **(a-b)**; or with GTP **(c-d)**. Bars = 100 nm.

Kalia, et al.
Extended Data Fig. 15

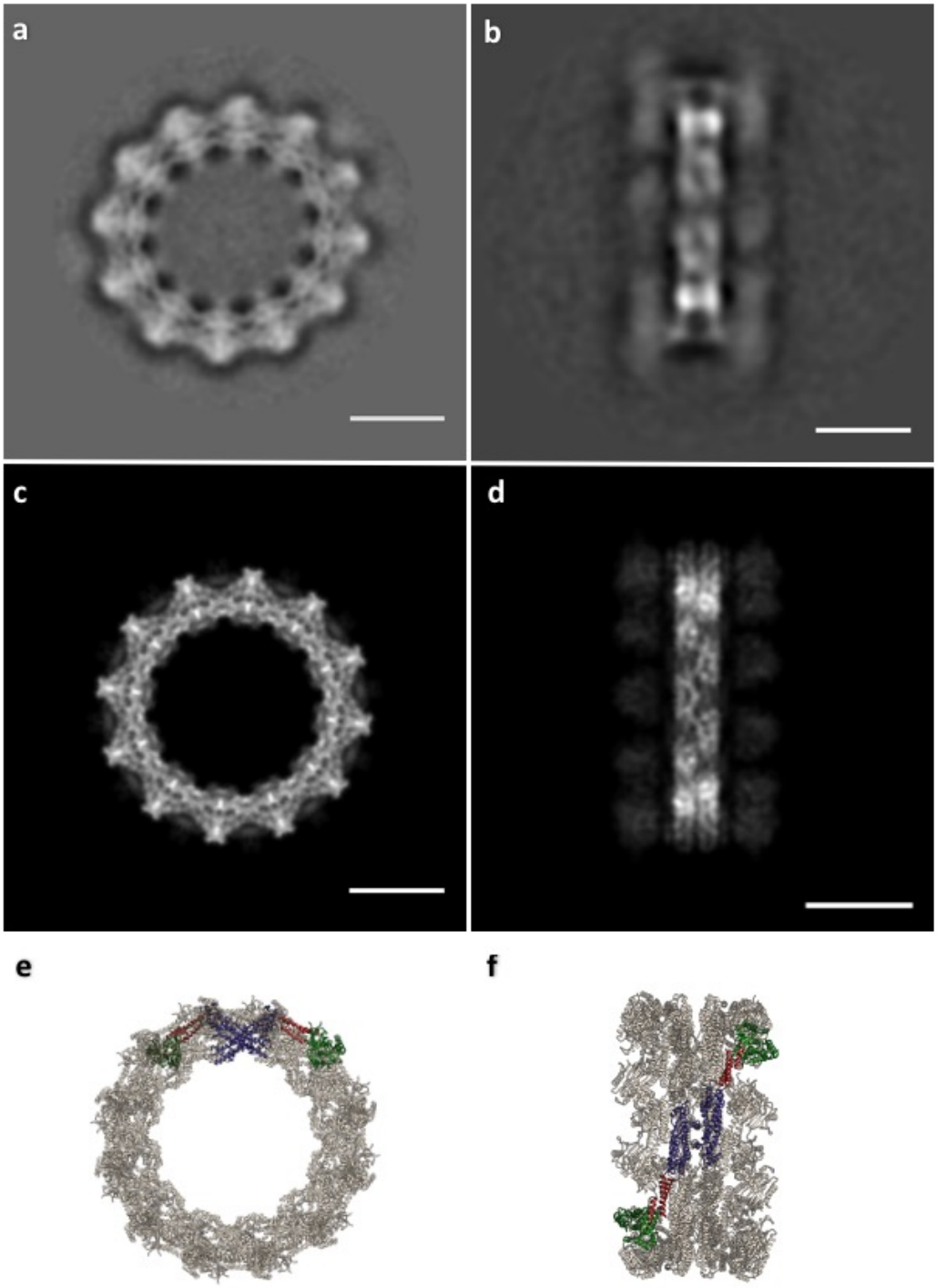

Extended data figure 15: $DRP1_{G362D}$ forms 12-dimer closed rings. **(a)** 2D class average of the rings; **(b)** 2D class average of infrequent, orthogonal or "side" views used as a constraint during model building; **(c)** "top" and **(d)** "side" projections of the model; **(e)** "top" and **(f)** "side" views of the final model rendered as ribbons. Bars =100Å. Green: G-domain, Red: Bundle Signaling Element (BSE), Purple: Stalk region.

Extended data movie Legends

Extended data movie 1: Nucleotide-induced conformational changes in the G-domain and Bundle Signaling Element (BSE).

Extended data movie 2: Nucleotide-induced conformational changes in the G-domain and Bundle Signaling Element (BSE) in the context of a full-length DRP1 dimer ("side" view).

Extended data movie 3: Nucleotide-induced conformational changes in the G-domain and Bundle Signaling Element (BSE) in the context of a full-length DRP1 dimer ("top" view).

Extended data movie 4: MID receptors engage a specific nucleotide-bound conformation of DRP1 tetramers and promote formation of a linear copolymer. Subsequent nucleotide hydrolysis and exchange promotes receptor dissociation and tetramer bending in the closed rings.

Extended data References

1 Gibson, D. G. *et al.* Enzymatic assembly of DNA molecules up to several hundred kilobases. *Nat Methods* **6**, 343-345, doi:10.1038/nmeth.1318 (2009).

2 Kalia, R., Talledge, N. & Frost, A. Structural and functional studies of membrane remodeling machines. *Methods in cell biology* **128**, 165-200, doi:10.1016/bs.mcb.2015.02.007 (2015).

3 Blommel, P. G., Becker, K. J., Duvnjak, P. & Fox, B. G. Enhanced Bacterial Protein Expression During Auto-induction Obtained by Alteration of Lac Repressor Dosage and Medium Composition. *Biotechnol Prog* **23**, 585-598, doi:10.1021/bp070011x (2007).

4 Studier, F. W. Protein production by auto-induction in high density shaking cultures. *Protein Expr Purif* **41**, 207-234 (2005).

5 Frohlich, C. *et al.* Structural insights into oligomerization and mitochondrial remodelling of dynamin 1-like protein. *Embo J* **32**, 1280-1292, doi:10.1038/emboj.2013.74 (2013).

6 Loson, O. C. *et al.* Crystal structure and functional analysis of MiD49, a receptor for the mitochondrial fission protein Drp1. *Protein Sci* **24**, 386-394, doi:10.1002/pro.2629 (2015).

7 Mastronarde, D. N. Automated electron microscope tomography using robust prediction of specimen movements. *Journal of structural biology* **152**, 36-51 (2005).

8 Zheng, S. Q. *et al.* MotionCor2: anisotropic correction of beam-induced motion for improved cryo-electron microscopy. *Nat Methods* **14**, 331-332, doi:10.1038/nmeth.4193 (2017).

9 Zhang, K. Gctf: Real-time CTF determination and correction. *Journal of structural biology* **193**, 1-12, doi:10.1016/j.jsb.2015.11.003 (2016).

10 Rohou, A. & Grigorieff, N. CTFFIND4: Fast and accurate defocus estimation from electron micrographs. *Journal of structural biology* **192**, 216-221, doi:10.1016/j.jsb.2015.08.008 (2015).

11 Bell, J. M., Chen, M., Baldwin, P. R. & Ludtke, S. J. High resolution single particle refinement in EMAN2.1. *Methods* **100**, 25-34, doi:10.1016/j.ymeth.2016.02.018 (2016).

12 Scheres, S. H. W. Semi-automated selection of cryo-EM particles in RELION-1.3. *Journal of structural biology* **189**, 114-122, doi:10.1016/j.jsb.2014.11.010 (2015).

13 Egelman, E. H. Reconstruction of helical filaments and tubes. *Methods Enzymol* **482**, 167-183, doi:10.1016/S0076-6879(10)82006-3 (2010).

14 Ge, P. *et al.* Cryo-EM model of the bullet-shaped vesicular stomatitis virus. *Science (New York, N.Y.)* **327**, 689-693, doi:10.1126/science.1181766 (2010).

15 Pintilie, G. D., Zhang, J., Goddard, T. D., Chiu, W. & Gossard, D. C. Quantitative analysis of cryo-EM density map segmentation by watershed and scale-space filtering, and fitting of structures by alignment to regions. *Journal of structural biology* **170**, 427-438, doi:10.1016/j.jsb.2010.03.007 (2010).

16 Goddard, T. D., Huang, C. C. & Ferrin, T. E. Visualizing density maps with UCSF Chimera. *Journal of structural biology* **157**, 281-287, doi:10.1016/j.jsb.2006.06.010 (2007).

17 Goddard, T. D., Huang, C. C. & Ferrin, T. E. Software extensions to UCSF chimera for interactive visualization of large molecular assemblies. *Structure* **13**, 473-482, doi:10.1016/j.str.2005.01.006 (2005).

18 Meng, E. C., Pettersen, E. F., Couch, G. S., Huang, C. C. & Ferrin, T. E. Tools for integrated sequence-structure analysis with UCSF Chimera. *BMC Bioinformatics* **7**, 339, doi:10.1186/1471-2105-7-339 (2006).
19 Pettersen, E. F. *et al.* UCSF Chimera--a visualization system for exploratory research and analysis. *J Comput Chem* **25**, 1605-1612, doi:10.1002/jcc.20084 (2004).
20 Wang, R. Y. *et al.* Automated structure refinement of macromolecular assemblies from cryo-EM maps using Rosetta. *eLife* **5**, doi:10.7554/eLife.17219 (2016).
21 Song, Y. *et al.* High-resolution comparative modeling with RosettaCM. *Structure* **21**, 1735-1742, doi:10.1016/j.str.2013.08.005 (2013).
22 DiMaio, F., Leaver-Fay, A., Bradley, P., Baker, D. & Andre, I. Modeling symmetric macromolecular structures in Rosetta3. *PloS one* **6**, e20450, doi:10.1371/journal.pone.0020450 (2011).
23 DiMaio, F. *et al.* Atomic-accuracy models from 4.5-A cryo-electron microscopy data with density-guided iterative local refinement. *Nature methods* **12**, 361-365, doi:10.1038/nmeth.3286 (2015).
24 Adams, P. D. *et al.* PHENIX: a comprehensive Python-based system for macromolecular structure solution. *Acta crystallographica. Section D, Biological crystallography* **66**, 213-221, doi:10.1107/S0907444909052925 (2010).
25 Kucukelbir, A., Sigworth, F. J. & Tagare, H. D. Quantifying the local resolution of cryo-EM density maps. *Nat Methods* **11**, 63-65, doi:10.1038/nmeth.2727 (2014).
26 Reubold, T. F. *et al.* Crystal structure of the dynamin tetramer. *Nature* **525**, 404-408, doi:10.1038/nature14880 (2015).

Full wwPDB/EMDataBank EM Map/Model Validation Report (i)

Aug 2, 2017 – 01:55 PM EDT

This is a Full wwPDB/EMDataBank EM Map/Model Validation Report.

This report is produced by the standalone wwPDB validation server.
The structure in question has not been deposited to the wwPDB.
This report should not be submitted to journals.

We welcome your comments at *validation@mail.wwpdb.org*
A user guide is available at
http://wwpdb.org/validation/2016/EMValidationReportHelp
with specific help available everywhere you see the (i) symbol.

PRELIMINARY VALIDATION REPORT

MolProbity	:	4.02b-467
Percentile statistics	:	20161228.v01 (using entries in the PDB archive December 28th 2016)
Ideal geometry (proteins)	:	Engh & Huber (2001)
Ideal geometry (DNA, RNA)	:	Parkinson et. al. (1996)
Validation Pipeline (wwPDB-VP)	:	rb-20029824

1 Overall quality at a glance (i)

The following experimental techniques were used to determine the structure:
ELECTRON MICROSCOPY

The reported resolution of this entry is unknown.

Percentile scores (ranging between 0-100) for global validation metrics of the entry are shown in the following graphic. The table shows the number of entries on which the scores are based.

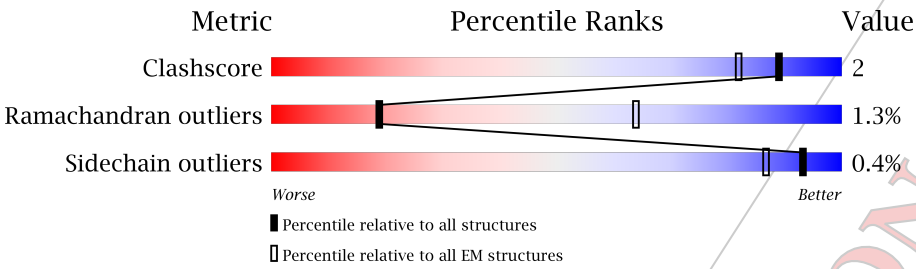

Metric	Whole archive (#Entries)	EM structures (#Entries)
Clashscore	125131	1336
Ramachandran outliers	121729	1120
Sidechain outliers	121581	1026

The table below summarises the geometric issues observed across the polymeric chains. The red, orange, yellow and green segments on the bar indicate the fraction of residues that contain outliers for >=3, 2, 1 and 0 types of geometric quality criteria. A grey segment represents the fraction of residues that are not modelled. The numeric value for each fraction is indicated below the corresponding segment, with a dot representing fractions <=5%

Mol	Chain	Length	Quality of chain
1	A	591	94% • •
1	C	591	94% • •
1	E	591	94% 5% •
1	G	591	94% 5% •
1	I	591	94% • •
1	K	591	94% 5% •
1	M	591	95% • •
1	O	591	95% • •
2	B	329	97% •

Continued on next page...

PRELIMINARY VALIDATION REPORT

Continued from previous page...

Mol	Chain	Length	Quality of chain
2	D	329	95% 5%
2	F	329	95% .
2	H	329	95% 5%
2	J	329	97% .
2	L	329	96% .
2	N	329	95% 5%
2	P	329	96% .

PRELIMINARY VALIDATION REPORT

2 Entry composition (i)

There are 2 unique types of molecules in this entry. The entry contains 116960 atoms, of which 59040 are hydrogens and 0 are deuteriums.

In the tables below, the AltConf column contains the number of residues with at least one atom in alternate conformation and the Trace column contains the number of residues modelled with at most 2 atoms.

- Molecule 1 is a protein.

Mol	Chain	Residues	Atoms								AltConf	Trace
			Total	C	H	Mg	N	O	P	S		
1	A	591	9493	2954	4801	1	821	893	3	20	0	1
1	C	591	9493	2954	4801	1	821	893	3	20	0	1
1	E	591	9493	2954	4801	1	821	893	3	20	0	1
1	G	591	9493	2954	4801	1	821	893	3	20	0	1
1	I	591	9493	2954	4801	1	821	893	3	20	0	1
1	K	591	9493	2954	4801	1	821	893	3	20	0	1
1	M	591	9493	2954	4801	1	821	893	3	20	0	1
1	O	591	9493	2954	4801	1	821	893	3	20	0	1

- Molecule 2 is a protein.

Mol	Chain	Residues	Atoms						AltConf	Trace
			Total	C	H	N	O	S		
2	B	329	5127	1630	2579	445	465	8	0	0
2	D	329	5127	1630	2579	445	465	8	0	0
2	F	329	5127	1630	2579	445	465	8	0	0
2	H	329	5127	1630	2579	445	465	8	0	0
2	J	329	5127	1630	2579	445	465	8	0	0
2	L	329	5127	1630	2579	445	465	8	0	0
2	N	329	5127	1630	2579	445	465	8	0	0

Continued on next page...

PRELIMINARY VALIDATION REPORT

Continued from previous page...

Mol	Chain	Residues	Atoms						AltConf	Trace
			Total	C	H	N	O	S		
2	P	329	5127	1630	2579	445	465	8	0	0

PRELIMINARY VALIDATION REPORT

3 Residue-property plots (i)

These plots are drawn for all protein, RNA and DNA chains in the entry. The first graphic for a chain summarises the proportions of the various outlier classes displayed in the second graphic. The second graphic shows the sequence view annotated by issues in geometry. Residues are color-coded according to the number of geometric quality criteria for which they contain at least one outlier: green = 0, yellow = 1, orange = 2 and red = 3 or more. Stretches of 2 or more consecutive residues without any outlier are shown as a green connector. Residues present in the sample, but not in the model, are shown in grey.

- Molecule 1:

Chain A:

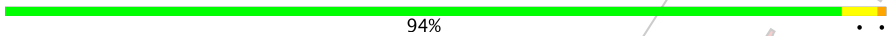

- Molecule 1:

Chain C:

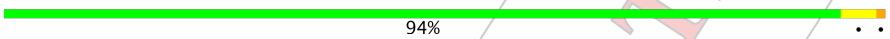

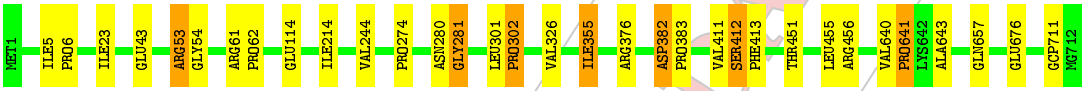

- Molecule 1:

Chain E:

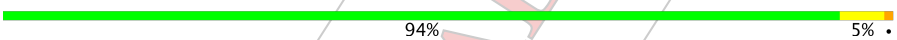

- Molecule 1:

Chain G:

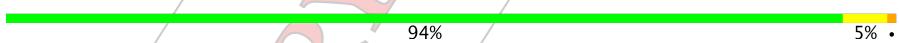

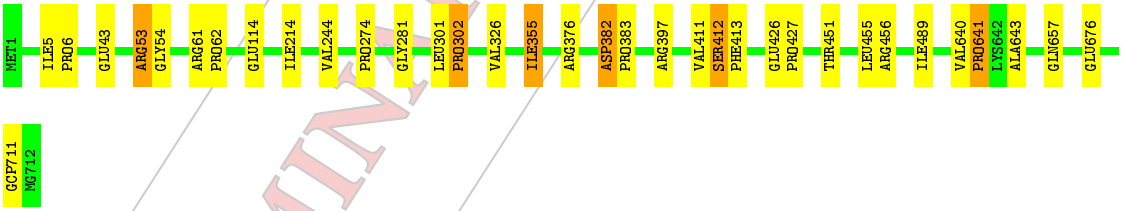

- Molecule 1:

Chain I:

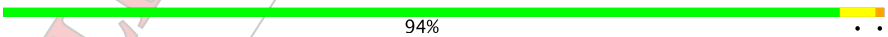

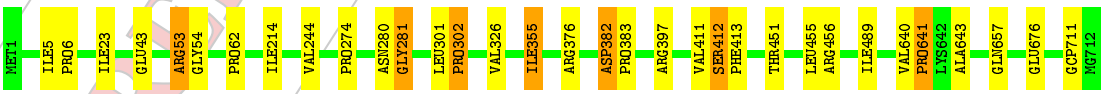

- Molecule 1:

PRELIMINARY VALIDATION REPORT

Chain K: 94% 5%

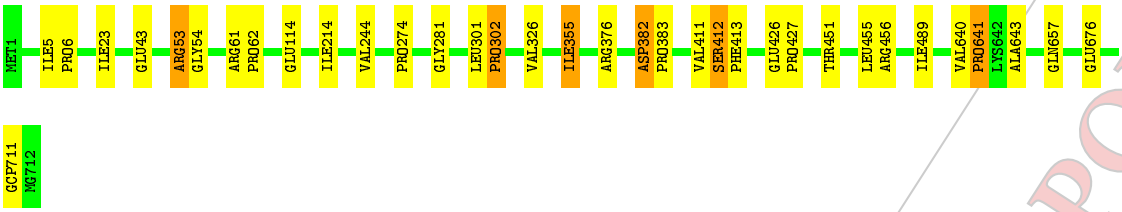

- Molecule 1:

Chain M: 95%

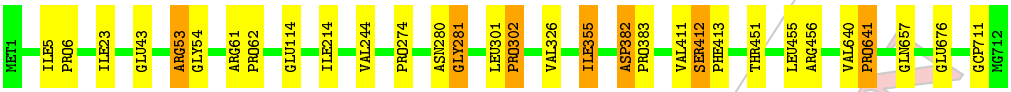

- Molecule 1:

Chain O: 95%

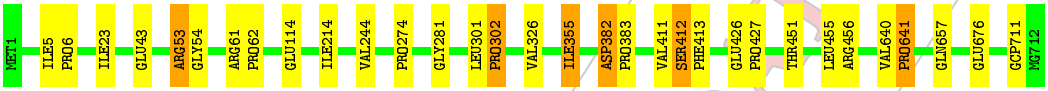

- Molecule 2:

Chain B: 97%

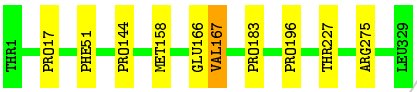

- Molecule 2:

Chain D: 95% 5%

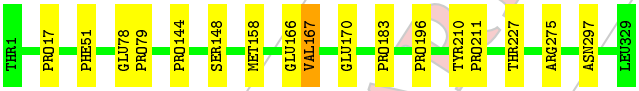

- Molecule 2:

Chain F: 95%

- Molecule 2:

Chain H: 95% 5%

PRELIMINARY VALIDATION REPORT

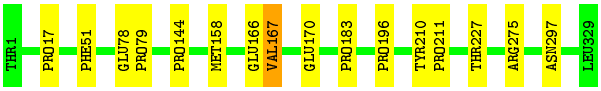

- Molecule 2:

Chain J: 97%

- Molecule 2:

Chain L: 96%

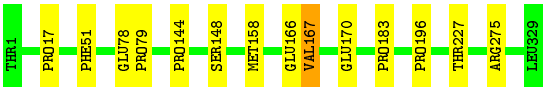

- Molecule 2:

Chain N: 95% 5%

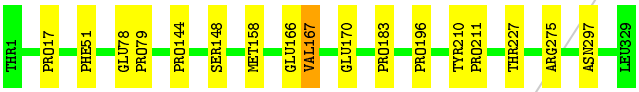

- Molecule 2:

Chain P: 96%

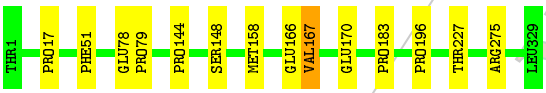

PRELIMINARY VALIDATION REPORT

4 Experimental information (i)

Property	Value	Source
Reconstruction method	Not provided	Depositor
Imposed symmetry	POINT, Not provided	Depositor
Number of images used	Not provided	Depositor
Resolution determination method	Not provided	Depositor
CTF correction method	Not provided	Depositor
Microscope	Not provided	Depositor
Voltage (kV)	Not provided	Depositor
Electron dose ($e^-/Å^2$)	Not provided	Depositor
Minimum defocus (nm)	Not provided	Depositor
Maximum defocus (nm)	Not provided	Depositor
Magnification	Not provided	Depositor
Image detector	Not provided	Depositor

PRELIMINARY VALIDATION REPORT

5 Model quality (i)

5.1 Standard geometry (i)

Bond lengths and bond angles in the following residue types are not validated in this section: GCP, MG

The Z score for a bond length (or angle) is the number of standard deviations the observed value is removed from the expected value. A bond length (or angle) with $|Z| > 5$ is considered an outlier worth inspection. RMSZ is the root-mean-square of all Z scores of the bond lengths (or angles).

Mol	Chain	Bond lengths		Bond angles	
		RMSZ	$\#\|Z\| >2$	RMSZ	$\#\|Z\| >2$
1	A	0.72	0/4727	0.51	0/6400
1	C	0.72	0/4727	0.51	0/6400
1	E	0.72	0/4727	0.51	0/6400
1	G	0.72	0/4727	0.51	0/6400
1	I	0.72	0/4727	0.51	0/6400
1	K	0.72	0/4727	0.51	0/6400
1	M	0.72	0/4727	0.51	0/6400
1	O	0.72	0/4727	0.51	0/6400
2	B	0.72	0/2601	0.49	0/3543
2	D	0.72	0/2601	0.49	0/3543
2	F	0.73	0/2601	0.49	0/3543
2	H	0.72	0/2601	0.49	0/3543
2	J	0.72	0/2601	0.49	0/3543
2	L	0.72	0/2601	0.49	0/3543
2	N	0.72	0/2601	0.49	0/3543
2	P	0.72	0/2601	0.49	0/3543
All	All	0.72	0/58624	0.50	0/79544

There are no bond length outliers.

There are no bond angle outliers.

There are no chirality outliers.

There are no planarity outliers.

5.2 Too-close contacts (i)

In the following table, the Non-H and H(model) columns list the number of non-hydrogen atoms and hydrogen atoms in the chain respectively. The H(added) column lists the number of hydrogen atoms added and optimized by MolProbity. The Clashes column lists the number of clashes within the asymmetric unit, whereas Symm-Clashes lists symmetry related clashes.

PRELIMINARY VALIDATION REPORT

Mol	Chain	Non-H	H(model)	H(added)	Clashes	Symm-Clashes
1	A	4692	4801	4813	27	0
1	C	4692	4801	4813	25	0
1	E	4692	4801	4813	24	0
1	G	4692	4801	4813	26	0
1	I	4692	4801	4813	25	0
1	K	4692	4801	4813	26	0
1	M	4692	4801	4813	23	0
1	O	4692	4801	4813	23	0
2	B	2548	2579	2581	5	0
2	D	2548	2579	2581	10	0
2	F	2548	2579	2581	8	0
2	H	2548	2579	2581	9	0
2	J	2548	2579	2581	5	0
2	L	2548	2579	2581	9	0
2	N	2548	2579	2581	10	0
2	P	2548	2579	2581	9	0
All	All	57920	59040	59152	249	0

The all-atom clashscore is defined as the number of clashes found per 1000 atoms (including hydrogen atoms). The all-atom clashscore for this structure is 2.

All (249) close contacts within the same asymmetric unit are listed below, sorted by their clash magnitude.

Atom-1	Atom-2	Interatomic distance (Å)	Clash overlap (Å)
1:A:657:GLN:OE1	1:A:657:GLN:N	2.15	0.80
1:C:657:GLN:OE1	1:C:657:GLN:N	2.15	0.80
1:M:657:GLN:OE1	1:M:657:GLN:N	2.14	0.80
1:O:657:GLN:OE1	1:O:657:GLN:N	2.15	0.79
1:K:657:GLN:OE1	1:K:657:GLN:N	2.14	0.79
1:G:657:GLN:OE1	1:G:657:GLN:N	2.15	0.79
1:E:657:GLN:N	1:E:657:GLN:OE1	2.15	0.79
1:O:355:ILE:HG22	1:O:355:ILE:O	1.83	0.77
1:I:657:GLN:N	1:I:657:GLN:OE1	2.15	0.77
1:K:355:ILE:O	1:K:355:ILE:HG22	1.83	0.77
1:E:355:ILE:HG22	1:E:355:ILE:O	1.83	0.77
1:M:355:ILE:HG22	1:M:355:ILE:O	1.83	0.77
1:G:355:ILE:O	1:G:355:ILE:HG22	1.83	0.76
1:C:355:ILE:HG22	1:C:355:ILE:O	1.83	0.76
1:A:355:ILE:HG22	1:A:355:ILE:O	1.83	0.76
1:I:355:ILE:O	1:I:355:ILE:HG22	1.83	0.75
1:E:397:ARG:NH1	2:L:148:SER:OG	2.30	0.65
2:D:227:THR:OG1	2:D:275:ARG:NH2	2.31	0.64

Continued on next page...

PRELIMINARY VALIDATION REPORT

Continued from previous page...

Atom-1	Atom-2	Interatomic distance (Å)	Clash overlap (Å)
2:J:167:VAL:O	2:J:167:VAL:HG13	1.96	0.64
2:N:227:THR:OG1	2:N:275:ARG:NH2	2.31	0.64
2:B:227:THR:OG1	2:B:275:ARG:NH2	2.31	0.64
2:J:227:THR:OG1	2:J:275:ARG:NH2	2.31	0.64
2:B:167:VAL:O	2:B:167:VAL:HG13	1.97	0.64
2:D:167:VAL:O	2:D:167:VAL:HG13	1.96	0.64
2:D:148:SER:OG	1:I:397:ARG:NH1	2.31	0.64
2:L:227:THR:OG1	2:L:275:ARG:NH2	2.31	0.64
2:H:227:THR:OG1	2:H:275:ARG:NH2	2.31	0.64
2:F:227:THR:OG1	2:F:275:ARG:NH2	2.31	0.63
2:P:167:VAL:HG13	2:P:167:VAL:O	1.96	0.63
2:P:227:THR:OG1	2:P:275:ARG:NH2	2.31	0.63
2:N:167:VAL:HG13	2:N:167:VAL:O	1.96	0.63
2:L:167:VAL:O	2:L:167:VAL:HG13	1.96	0.63
2:H:167:VAL:HG13	2:H:167:VAL:O	1.96	0.63
2:F:167:VAL:O	2:F:167:VAL:HG13	1.96	0.62
1:I:43:GLU:OE1	1:I:43:GLU:HA	2.02	0.58
1:O:43:GLU:HA	1:O:43:GLU:OE1	2.03	0.58
1:A:43:GLU:OE1	1:A:43:GLU:HA	2.03	0.58
1:K:43:GLU:HA	1:K:43:GLU:OE1	2.02	0.58
1:C:43:GLU:HA	1:C:43:GLU:OE1	2.03	0.57
1:E:43:GLU:OE1	1:E:43:GLU:HA	2.03	0.57
1:G:43:GLU:OE1	1:G:43:GLU:HA	2.03	0.57
1:M:43:GLU:OE1	1:M:43:GLU:HA	2.02	0.57
1:A:397:ARG:NH1	2:N:148:SER:OG	2.40	0.55
1:G:397:ARG:NH1	2:P:148:SER:OG	2.40	0.55
1:A:382:ASP:CB	1:A:383:PRO:HA	2.39	0.52
1:I:382:ASP:CB	1:I:383:PRO:HA	2.39	0.52
1:C:382:ASP:CB	1:C:383:PRO:HA	2.39	0.52
1:M:382:ASP:CB	1:M:383:PRO:HA	2.39	0.52
1:E:382:ASP:CB	1:E:383:PRO:HA	2.39	0.51
1:G:382:ASP:CB	1:G:383:PRO:HA	2.39	0.51
1:K:382:ASP:CB	1:K:383:PRO:HA	2.39	0.51
1:O:382:ASP:CB	1:O:383:PRO:HA	2.39	0.51
1:I:214:ILE:O	1:I:244:VAL:N	2.44	0.50
1:A:214:ILE:O	1:A:244:VAL:N	2.44	0.49
1:M:214:ILE:O	1:M:244:VAL:N	2.44	0.49
2:B:51:PHE:CD1	2:B:51:PHE:N	2.80	0.49
1:C:214:ILE:O	1:C:244:VAL:N	2.44	0.49
2:D:51:PHE:CD1	2:D:51:PHE:N	2.80	0.49
1:K:214:ILE:O	1:K:244:VAL:N	2.44	0.49

Continued on next page...

PRELIMINARY VALIDATION REPORT

Continued from previous page...

Atom-1	Atom-2	Interatomic distance (Å)	Clash overlap (Å)
1:G:214:ILE:O	1:G:244:VAL:N	2.44	0.49
1:O:214:ILE:O	1:O:244:VAL:N	2.44	0.49
2:N:51:PHE:N	2:N:51:PHE:CD1	2.80	0.49
1:E:214:ILE:O	1:E:244:VAL:N	2.44	0.48
1:C:412:SER:OG	1:C:413:PHE:N	2.47	0.48
1:E:376:ARG:O	2:H:158:MET:SD	2.72	0.48
2:B:158:MET:SD	1:I:376:ARG:O	2.71	0.48
2:J:51:PHE:N	2:J:51:PHE:CD1	2.80	0.48
1:A:412:SER:OG	1:A:413:PHE:N	2.47	0.48
1:E:412:SER:OG	1:E:413:PHE:N	2.47	0.48
1:G:412:SER:OG	1:G:413:PHE:N	2.47	0.48
1:I:412:SER:OG	1:I:413:PHE:N	2.47	0.48
1:K:412:SER:OG	1:K:413:PHE:N	2.47	0.47
1:O:412:SER:OG	1:O:413:PHE:N	2.47	0.47
2:F:51:PHE:N	2:F:51:PHE:CD1	2.80	0.47
2:L:51:PHE:CD1	2:L:51:PHE:N	2.80	0.47
2:P:51:PHE:CD1	2:P:51:PHE:N	2.80	0.47
1:E:54:GLY:O	1:E:711:GCP:H5'1	2.14	0.47
2:H:51:PHE:N	2:H:51:PHE:CD1	2.80	0.47
1:G:54:GLY:O	1:G:711:GCP:H5'1	2.14	0.47
1:K:640:VAL:N	1:K:641:PRO:CD	2.78	0.47
1:K:54:GLY:O	1:K:711:GCP:H5'1	2.14	0.47
1:O:640:VAL:N	1:O:641:PRO:CD	2.78	0.47
1:G:640:VAL:N	1:G:641:PRO:CD	2.78	0.46
1:E:640:VAL:N	1:E:641:PRO:CD	2.78	0.46
1:O:54:GLY:O	1:O:711:GCP:H5'1	2.14	0.46
1:I:54:GLY:O	1:I:711:GCP:H5'1	2.14	0.46
1:M:54:GLY:O	1:M:711:GCP:H5'1	2.14	0.46
1:A:54:GLY:O	1:A:711:GCP:H5'1	2.14	0.46
1:A:640:VAL:N	1:A:641:PRO:CD	2.78	0.46
1:C:54:GLY:O	1:C:711:GCP:H5'1	2.14	0.46
1:C:640:VAL:N	1:C:641:PRO:CD	2.78	0.46
1:I:640:VAL:N	1:I:641:PRO:CD	2.78	0.46
1:M:640:VAL:N	1:M:641:PRO:CD	2.78	0.46
1:G:376:ARG:O	2:L:158:MET:SD	2.74	0.46
1:E:640:VAL:HB	1:E:641:PRO:HD3	1.98	0.46
1:G:640:VAL:HB	1:G:641:PRO:HD3	1.98	0.46
1:K:640:VAL:HB	1:K:641:PRO:HD3	1.98	0.46
1:M:640:VAL:HB	1:M:641:PRO:HD3	1.98	0.45
1:O:640:VAL:HB	1:O:641:PRO:HD3	1.98	0.45
1:A:382:ASP:CB	1:A:383:PRO:CA	2.94	0.45

Continued on next page...

PRELIMINARY VALIDATION REPORT

Continued from previous page...

Atom-1	Atom-2	Interatomic distance (Å)	Clash overlap (Å)
1:I:382:ASP:CB	1:I:383:PRO:CA	2.95	0.45
1:C:382:ASP:CB	1:C:383:PRO:CA	2.94	0.45
1:A:489:ILE:HD12	1:G:643:ALA:HA	1.98	0.45
1:E:5:ILE:HB	1:E:6:PRO:CD	2.47	0.45
1:G:5:ILE:HB	1:G:6:PRO:CD	2.47	0.45
1:K:5:ILE:HB	1:K:6:PRO:CD	2.47	0.45
1:M:382:ASP:CB	1:M:383:PRO:CA	2.94	0.45
1:C:640:VAL:HB	1:C:641:PRO:HD3	1.98	0.45
1:E:382:ASP:CB	1:E:383:PRO:CA	2.94	0.45
1:O:382:ASP:CB	1:O:383:PRO:CA	2.94	0.45
1:O:5:ILE:HB	1:O:6:PRO:CD	2.47	0.45
1:G:382:ASP:CB	1:G:383:PRO:CA	2.95	0.45
1:A:640:VAL:HB	1:A:641:PRO:HD3	1.98	0.45
1:M:5:ILE:HB	1:M:6:PRO:CD	2.47	0.45
1:K:382:ASP:CB	1:K:383:PRO:CA	2.95	0.45
1:C:5:ILE:HB	1:C:6:PRO:CD	2.47	0.45
1:E:355:ILE:CG2	1:E:355:ILE:O	2.56	0.45
1:A:643:ALA:HA	1:G:489:ILE:HD12	1.98	0.45
1:I:640:VAL:HB	1:I:641:PRO:HD3	1.98	0.45
1:G:355:ILE:CG2	1:G:355:ILE:O	2.56	0.44
1:A:5:ILE:HB	1:A:6:PRO:CD	2.47	0.44
2:D:166:GLU:O	2:D:167:VAL:HB	2.18	0.44
1:I:643:ALA:HA	1:K:489:ILE:HD12	1.99	0.44
1:I:5:ILE:HB	1:I:6:PRO:CD	2.47	0.44
2:B:166:GLU:O	2:B:167:VAL:HB	2.18	0.44
1:K:355:ILE:CG2	1:K:355:ILE:O	2.56	0.44
2:N:166:GLU:O	2:N:167:VAL:HB	2.18	0.44
1:G:411:VAL:O	1:G:412:SER:C	2.57	0.44
2:J:166:GLU:O	2:J:167:VAL:HB	2.18	0.44
1:K:411:VAL:O	1:K:412:SER:C	2.57	0.44
1:O:355:ILE:O	1:O:355:ILE:CG2	2.56	0.44
1:A:355:ILE:O	1:A:355:ILE:CG2	2.56	0.43
1:E:411:VAL:O	1:E:412:SER:C	2.57	0.43
2:F:166:GLU:O	2:F:167:VAL:HB	2.18	0.43
1:O:411:VAL:O	1:O:412:SER:C	2.57	0.43
2:H:166:GLU:O	2:H:167:VAL:HB	2.18	0.43
2:L:166:GLU:O	2:L:167:VAL:HB	2.18	0.43
2:P:166:GLU:O	2:P:167:VAL:HB	2.18	0.43
1:A:382:ASP:HB3	1:A:383:PRO:CA	2.49	0.43
1:C:355:ILE:O	1:C:355:ILE:CG2	2.56	0.43
1:C:382:ASP:HB3	1:C:383:PRO:CA	2.49	0.43

Continued on next page...

PRELIMINARY VALIDATION REPORT

Continued from previous page...

Atom-1	Atom-2	Interatomic distance (Å)	Clash overlap (Å)
1:M:382:ASP:HB3	1:M:383:PRO:CA	2.49	0.43
1:M:355:ILE:O	1:M:355:ILE:CG2	2.56	0.43
1:I:382:ASP:HB3	1:I:383:PRO:CA	2.49	0.43
1:I:411:VAL:O	1:I:412:SER:C	2.57	0.43
1:A:411:VAL:O	1:A:412:SER:C	2.57	0.43
2:P:78:GLU:HA	2:P:79:PRO:HD3	1.87	0.43
1:E:382:ASP:HB3	1:E:383:PRO:CA	2.49	0.43
1:C:411:VAL:O	1:C:412:SER:C	2.57	0.42
1:G:382:ASP:HB3	1:G:383:PRO:CA	2.49	0.42
1:I:489:ILE:HD12	1:K:643:ALA:HA	2.01	0.42
1:O:382:ASP:HB3	1:O:383:PRO:CA	2.49	0.42
2:L:78:GLU:HA	2:L:79:PRO:HD3	1.87	0.42
1:M:411:VAL:O	1:M:412:SER:C	2.57	0.42
1:A:376:ARG:O	2:D:158:MET:SD	2.77	0.42
1:K:382:ASP:HB3	1:K:383:PRO:CA	2.49	0.42
1:C:376:ARG:O	2:N:158:MET:SD	2.77	0.42
1:A:451:THR:O	1:A:455:LEU:N	2.53	0.42
1:I:451:THR:O	1:I:455:LEU:N	2.53	0.42
1:C:451:THR:O	1:C:455:LEU:N	2.53	0.42
1:A:456:ARG:O	1:A:676:GLU:HA	2.20	0.42
2:H:78:GLU:HA	2:H:79:PRO:HD3	1.87	0.42
1:I:456:ARG:O	1:I:676:GLU:HA	2.20	0.42
1:M:412:SER:OG	1:M:413:PHE:N	2.47	0.42
1:M:451:THR:O	1:M:455:LEU:N	2.53	0.42
1:O:451:THR:O	1:O:455:LEU:N	2.53	0.42
1:K:451:THR:O	1:K:455:LEU:N	2.53	0.42
1:G:451:THR:O	1:G:455:LEU:N	2.53	0.41
1:C:456:ARG:O	1:C:676:GLU:HA	2.20	0.41
1:E:382:ASP:HB2	1:E:383:PRO:HA	2.02	0.41
1:E:451:THR:O	1:E:455:LEU:N	2.53	0.41
1:M:456:ARG:O	1:M:676:GLU:HA	2.20	0.41
1:I:53:ARG:N	1:I:53:ARG:HD2	2.36	0.41
1:C:382:ASP:HB2	1:C:383:PRO:HA	2.02	0.41
1:O:426:GLU:HB3	1:O:427:PRO:HD3	2.03	0.41
1:A:53:ARG:N	1:A:53:ARG:HD2	2.36	0.41
1:G:382:ASP:HB2	1:G:383:PRO:HA	2.02	0.41
1:I:23:ILE:HG23	1:I:23:ILE:O	2.20	0.41
1:O:53:ARG:HD2	1:O:53:ARG:N	2.36	0.41
1:A:382:ASP:HB2	1:A:383:PRO:HA	2.02	0.41
1:C:301:LEU:HB2	1:C:302:PRO:HD3	2.03	0.41
1:E:456:ARG:O	1:E:676:GLU:HA	2.20	0.41

Continued on next page...

PRELIMINARY VALIDATION REPORT

Continued from previous page...

Atom-1	Atom-2	Interatomic distance (Å)	Clash overlap (Å)
1:G:426:GLU:HB3	1:G:427:PRO:HD3	2.03	0.41
1:K:426:GLU:HB3	1:K:427:PRO:HD3	2.03	0.41
1:K:53:ARG:HD2	1:K:53:ARG:N	2.36	0.41
1:M:382:ASP:HB2	1:M:383:PRO:HA	2.02	0.41
1:A:23:ILE:O	1:A:23:ILE:HG23	2.20	0.41
1:A:301:LEU:HB2	1:A:302:PRO:HD3	2.03	0.41
1:C:53:ARG:HD2	1:C:53:ARG:N	2.36	0.41
1:C:643:ALA:HA	1:E:489:ILE:HD12	2.02	0.41
2:F:78:GLU:HA	2:F:79:PRO:HD3	1.87	0.41
1:K:456:ARG:O	1:K:676:GLU:HA	2.20	0.41
1:M:301:LEU:HB2	1:M:302:PRO:HD3	2.03	0.41
1:O:456:ARG:O	1:O:676:GLU:HA	2.20	0.41
1:C:382:ASP:HB3	1:C:383:PRO:HA	2.02	0.41
1:E:426:GLU:HB3	1:E:427:PRO:HD3	2.03	0.41
1:G:456:ARG:O	1:G:676:GLU:HA	2.20	0.41
1:I:280:ASN:O	1:I:281:GLY:C	2.59	0.41
1:I:382:ASP:HB2	1:I:383:PRO:HA	2.02	0.41
2:P:170:GLU:N	2:P:170:GLU:OE1	2.54	0.41
1:A:280:ASN:O	1:A:281:GLY:C	2.59	0.41
1:A:61:ARG:HA	1:A:62:PRO:HD3	1.94	0.41
1:C:23:ILE:O	1:C:23:ILE:HG23	2.20	0.41
1:G:53:ARG:N	1:G:53:ARG:HD2	2.36	0.41
2:L:170:GLU:OE1	2:L:170:GLU:N	2.54	0.41
1:M:382:ASP:HB3	1:M:383:PRO:HA	2.02	0.41
1:M:53:ARG:N	1:M:53:ARG:HD2	2.36	0.41
1:A:382:ASP:HB3	1:A:383:PRO:HA	2.02	0.41
2:H:170:GLU:N	2:H:170:GLU:OE1	2.54	0.41
1:I:301:LEU:HB2	1:I:302:PRO:HD3	2.03	0.41
2:P:167:VAL:CG1	2:P:167:VAL:O	2.65	0.41
1:C:280:ASN:O	1:C:281:GLY:C	2.60	0.41
2:F:170:GLU:OE1	2:F:170:GLU:N	2.54	0.41
1:G:301:LEU:HB2	1:G:302:PRO:HD3	2.03	0.41
1:K:382:ASP:HB2	1:K:383:PRO:HA	2.02	0.41
2:N:78:GLU:HA	2:N:79:PRO:HD3	1.87	0.41
1:O:23:ILE:O	1:O:23:ILE:HG23	2.20	0.41
1:O:382:ASP:HB3	1:O:383:PRO:HA	2.02	0.41
2:D:78:GLU:HA	2:D:79:PRO:HD3	1.87	0.40
2:J:167:VAL:O	2:J:167:VAL:CG1	2.65	0.40
1:O:61:ARG:NH1	1:O:114:GLU:O	2.54	0.40
1:E:53:ARG:HD2	1:E:53:ARG:N	2.36	0.40
1:I:382:ASP:HB3	1:I:383:PRO:HA	2.02	0.40

Continued on next page...

PRELIMINARY VALIDATION REPORT

Continued from previous page...

Atom-1	Atom-2	Interatomic distance (Å)	Clash overlap (Å)
1:K:382:ASP:HB3	1:K:383:PRO:HA	2.02	0.40
2:L:167:VAL:O	2:L:167:VAL:CG1	2.65	0.40
1:M:280:ASN:O	1:M:281:GLY:C	2.59	0.40
1:O:301:LEU:HB2	1:O:302:PRO:HD3	2.03	0.40
1:O:382:ASP:HB2	1:O:383:PRO:HA	2.02	0.40
2:F:297:ASN:C	2:F:297:ASN:OD1	2.60	0.40
1:K:301:LEU:HB2	1:K:302:PRO:HD3	2.03	0.40
1:M:61:ARG:NH1	1:M:114:GLU:O	2.54	0.40
1:M:23:ILE:HG23	1:M:23:ILE:O	2.20	0.40
1:C:61:ARG:NH1	1:C:114:GLU:O	2.54	0.40
2:D:297:ASN:C	2:D:297:ASN:OD1	2.60	0.40
1:E:301:LEU:HB2	1:E:302:PRO:HD3	2.03	0.40
1:G:61:ARG:NH1	1:G:114:GLU:O	2.54	0.40
1:K:61:ARG:NH1	1:K:114:GLU:O	2.54	0.40
1:K:23:ILE:HG23	1:K:23:ILE:O	2.20	0.40
2:N:170:GLU:OE1	2:N:170:GLU:N	2.54	0.40
2:D:170:GLU:N	2:D:170:GLU:OE1	2.54	0.40
2:D:210:TYR:N	2:D:211:PRO:HD2	2.37	0.40
1:E:61:ARG:NH1	1:E:114:GLU:O	2.54	0.40
2:F:210:TYR:N	2:F:211:PRO:HD2	2.37	0.40
1:G:382:ASP:HB3	1:G:383:PRO:HA	2.02	0.40
2:H:210:TYR:N	2:H:211:PRO:HD2	2.36	0.40
2:H:297:ASN:OD1	2:H:297:ASN:C	2.60	0.40
2:N:210:TYR:N	2:N:211:PRO:HD2	2.36	0.40
2:N:297:ASN:C	2:N:297:ASN:OD1	2.60	0.40
1:K:376:ARG:O	2:P:158:MET:SD	2.80	0.40

There are no symmetry-related clashes.

5.3 Torsion angles (i)

5.3.1 Protein backbone (i)

In the following table, the Percentiles column shows the percent Ramachandran outliers of the chain as a percentile score with respect to all PDB entries followed by that with respect to all EM entries.

The Analysed column shows the number of residues for which the backbone conformation was analysed, and the total number of residues.

PRELIMINARY VALIDATION REPORT

Mol	Chain	Analysed	Favoured	Allowed	Outliers	Percentiles	
1	A	583/591 (99%)	550 (94%)	25 (4%)	8 (1%)	13	13
1	C	583/591 (99%)	550 (94%)	25 (4%)	8 (1%)	13	13
1	E	583/591 (99%)	550 (94%)	25 (4%)	8 (1%)	13	13
1	G	583/591 (99%)	550 (94%)	25 (4%)	8 (1%)	13	13
1	I	583/591 (99%)	550 (94%)	25 (4%)	8 (1%)	13	13
1	K	583/591 (99%)	550 (94%)	25 (4%)	8 (1%)	13	13
1	M	583/591 (99%)	550 (94%)	25 (4%)	8 (1%)	13	13
1	O	583/591 (99%)	550 (94%)	25 (4%)	8 (1%)	13	13
2	B	327/329 (99%)	302 (92%)	21 (6%)	4 (1%)	15	15
2	D	327/329 (99%)	302 (92%)	21 (6%)	4 (1%)	15	15
2	F	327/329 (99%)	302 (92%)	21 (6%)	4 (1%)	15	15
2	H	327/329 (99%)	302 (92%)	21 (6%)	4 (1%)	15	15
2	J	327/329 (99%)	302 (92%)	21 (6%)	4 (1%)	15	15
2	L	327/329 (99%)	302 (92%)	21 (6%)	4 (1%)	15	15
2	N	327/329 (99%)	302 (92%)	21 (6%)	4 (1%)	15	15
2	P	327/329 (99%)	302 (92%)	21 (6%)	4 (1%)	15	15
All	All	7280/7360 (99%)	6816 (94%)	368 (5%)	96 (1%)	19	14

All (96) Ramachandran outliers are listed below:

Mol	Chain	Res	Type
1	A	382	ASP
1	A	412	SER
2	B	167	VAL
1	C	382	ASP
1	C	412	SER
2	D	167	VAL
1	E	382	ASP
1	E	412	SER
2	F	167	VAL
1	G	382	ASP
1	G	412	SER
2	H	167	VAL
1	I	382	ASP
1	I	412	SER
2	J	167	VAL
1	K	382	ASP

Continued on next page...

PRELIMINARY VALIDATION REPORT

Continued from previous page...

Mol	Chain	Res	Type
1	K	412	SER
2	L	167	VAL
1	M	382	ASP
1	M	412	SER
2	N	167	VAL
1	O	382	ASP
1	O	412	SER
2	P	167	VAL
1	A	281	GLY
1	C	281	GLY
1	E	281	GLY
1	G	281	GLY
1	I	281	GLY
1	K	281	GLY
1	M	281	GLY
1	O	281	GLY
1	A	274	PRO
1	A	326	VAL
2	B	17	PRO
1	C	274	PRO
1	C	326	VAL
2	D	17	PRO
1	E	274	PRO
1	E	326	VAL
2	F	17	PRO
1	G	274	PRO
1	G	326	VAL
2	H	17	PRO
1	I	274	PRO
1	I	326	VAL
2	J	17	PRO
1	K	274	PRO
1	K	326	VAL
2	L	17	PRO
1	M	274	PRO
1	M	326	VAL
2	N	17	PRO
1	O	274	PRO
1	O	326	VAL
2	P	17	PRO
1	A	641	PRO
2	B	196	PRO

Continued on next page...

PRELIMINARY VALIDATION REPORT

Continued from previous page...

Mol	Chain	Res	Type
1	C	641	PRO
2	D	196	PRO
1	E	641	PRO
1	G	641	PRO
1	I	641	PRO
1	K	641	PRO
1	M	641	PRO
1	O	641	PRO
1	A	62	PRO
1	A	355	ILE
2	B	183	PRO
1	C	62	PRO
1	C	355	ILE
2	D	183	PRO
1	E	62	PRO
1	E	355	ILE
2	F	183	PRO
2	F	196	PRO
1	G	62	PRO
1	G	355	ILE
2	H	183	PRO
2	H	196	PRO
1	I	62	PRO
1	I	355	ILE
2	J	183	PRO
2	J	196	PRO
1	K	62	PRO
1	K	355	ILE
2	L	183	PRO
2	L	196	PRO
1	M	62	PRO
1	M	355	ILE
2	N	183	PRO
2	N	196	PRO
1	O	62	PRO
1	O	355	ILE
2	P	183	PRO
2	P	196	PRO

PRELIMINARY VALIDATION REPORT

5.3.2 Protein sidechains (i)

In the following table, the Percentiles column shows the percent sidechain outliers of the chain as a percentile score with respect to all PDB entries followed by that with respect to all EM entries.

The Analysed column shows the number of residues for which the sidechain conformation was analysed, and the total number of residues.

Mol	Chain	Analysed	Rotameric	Outliers	Percentiles	
1	A	527/527 (100%)	525 (100%)	2 (0%)	93	93
1	C	527/527 (100%)	525 (100%)	2 (0%)	93	93
1	E	527/527 (100%)	525 (100%)	2 (0%)	93	93
1	G	527/527 (100%)	525 (100%)	2 (0%)	93	93
1	I	527/527 (100%)	525 (100%)	2 (0%)	93	93
1	K	527/527 (100%)	525 (100%)	2 (0%)	93	93
1	M	527/527 (100%)	525 (100%)	2 (0%)	93	93
1	O	527/527 (100%)	525 (100%)	2 (0%)	93	93
2	B	268/268 (100%)	267 (100%)	1 (0%)	93	93
2	D	268/268 (100%)	267 (100%)	1 (0%)	93	93
2	F	268/268 (100%)	267 (100%)	1 (0%)	93	93
2	H	268/268 (100%)	267 (100%)	1 (0%)	93	93
2	J	268/268 (100%)	267 (100%)	1 (0%)	93	93
2	L	268/268 (100%)	267 (100%)	1 (0%)	93	93
2	N	268/268 (100%)	267 (100%)	1 (0%)	93	93
2	P	268/268 (100%)	267 (100%)	1 (0%)	93	93
All	All	6360/6360 (100%)	6336 (100%)	24 (0%)	93	93

All (24) residues with a non-rotameric sidechain are listed below:

Mol	Chain	Res	Type
1	A	53	ARG
1	A	302	PRO
2	B	144	PRO
1	C	53	ARG
1	C	302	PRO
2	D	144	PRO
1	E	53	ARG
1	E	302	PRO

Continued on next page...

PRELIMINARY VALIDATION REPORT

Continued from previous page...

Mol	Chain	Res	Type
2	F	144	PRO
1	G	53	ARG
1	G	302	PRO
2	H	144	PRO
1	I	53	ARG
1	I	302	PRO
2	J	144	PRO
1	K	53	ARG
1	K	302	PRO
2	L	144	PRO
1	M	53	ARG
1	M	302	PRO
2	N	144	PRO
1	O	53	ARG
1	O	302	PRO
2	P	144	PRO

Some sidechains can be flipped to improve hydrogen bonding and reduce clashes. There are no such sidechains identified.

5.3.3 RNA (i)

There are no RNA molecules in this entry.

5.4 Non-standard residues in protein, DNA, RNA chains (i)

There are no non-standard protein/DNA/RNA residues in this entry.

5.5 Carbohydrates (i)

There are no carbohydrates in this entry.

5.6 Ligand geometry (i)

There are no ligands in this entry.

5.7 Other polymers (i)

There are no such residues in this entry.

PRELIMINARY VALIDATION REPORT

5.8 Polymer linkage issues (i)

The following chains have linkage breaks:

Mol	Chain	Number of breaks
1	G	2
1	K	2
1	E	2
1	I	2
1	C	2
1	A	2
1	O	2
1	M	2

All chain breaks are listed below:

Model	Chain	Residue-1	Atom-1	Residue-2	Atom-2	Distance (Å)
1	A	503:ASP	C	612:ALA	N	20.73
1	C	503:ASP	C	612:ALA	N	20.73
1	E	503:ASP	C	612:ALA	N	20.73
1	G	503:ASP	C	612:ALA	N	20.73
1	I	503:ASP	C	612:ALA	N	20.73
1	K	503:ASP	C	612:ALA	N	20.73
1	M	503:ASP	C	612:ALA	N	20.73
1	O	503:ASP	C	612:ALA	N	20.73
1	A	73:GLU	C	87:ALA	N	9.30
1	C	73:GLU	C	87:ALA	N	9.30
1	E	73:GLU	C	87:ALA	N	9.30
1	G	73:GLU	C	87:ALA	N	9.30
1	I	73:GLU	C	87:ALA	N	9.30
1	K	73:GLU	C	87:ALA	N	9.30
1	M	73:GLU	C	87:ALA	N	9.30
1	O	73:GLU	C	87:ALA	N	9.30

PRELIMINARY VALIDATION REPORT